Applied Ocean Research 91 (2019) 101882

Contents lists available at ScienceDirect

Applied Ocean Research

journal homepage: www.elsevier.com/locate/apor

3D modelling of the impacts of in-stream horizontal-axis Tidal Energy Converters (TECs) on offshore sandbank dynamics

Antonia Chatzirodou[a,*], Harshinie Karunarathna[b], Dominic E. Reeve[b]

[a] Department of Geography and Environmental Management, University of West of England, UK
[b] Zienkiewickz Centre for Computational Engineering, College of Engineering, Bay Campus, Swansea University, Swansea, UK

ARTICLE INFO

Keywords:
Inner sound channel
Tidal energy converters
Environmental impacts
Morphodynamics
Offshore sandbanks
Delft3D

ABSTRACT

The tidal energy sector is a growing industry in the UK and beyond. Energy developers' interests are progressing towards the deployment of large arrays of tidal energy converters (TECs). Numerous factors will affect decision making related to arrays siting and size. One key factor is the effect that the TEC arrays may have on the natural sediment transport patterns and the sea bottom morphodynamics. The Inner Sound Channel located between the Island of Stroma of Pentland Firth and the Scottish Mainland (UK) has been accredited for a large-scale TEC array installation to be developed in the future. Three morphodynamically active, large sandbanks are located in the Inner Sound channel. This study investigated the impacts of tidal energy extraction from a large array of TECs on the sediment dynamics and morphology of these sandbanks. A large-scale 3D hydrodynamic and morphodynamic Delft3D model was set up to computationally model Pentland Firth, Inner Sound Channel in order to study the impacts of tidal energy extraction from a generic TEC array, on the existing hydrodynamic and morphodynamic regime. A range of hypothetical energy extraction scenarios was modelled. Results reveal that the changes to morphodynamics of these sandbanks as a result of large scale tidal energy extraction far exceeds the morphology change under the natural hydrodynamic regime and that the severity of morphology change depends on the level of energy extraction.

1. Introduction

Tidal stream technology has a reliable and promising power potential and has undergone intensive academic research over the past decade. Commercial interests have now moved towards planning of large arrays of tidal energy converter (TEC) deployments. Numerous factors, many quite uncertain at the moment and linked to site specifications, will determine the array location, size, layout and TEC operating characteristics. One such factor that will play an important role in decision making is the impact of TECs on the ambient marine environment (e.g. hydrodynamics; biological receptors; sediment transport dynamics) [1–4].

Numerical models are a well-established tool to study the impact of tidal energy extraction on the marine environment [5–8]. However, limited research has been done on the impact of TECs on sediment dynamics, due to the limited availability of natural sediment transport information at potential TEC deployment sites. However, potential changes to natural sediment transport processes and sea bottom morphodynamics as a result of the altered tidal flows in TEC array sites cannot be disregarded as they may also have significant impacts on the sea bed morphology and the marine ecological environment.

There are a few previous studies on the impact of tidal energy extraction on sediment transport. Neill et al. [9], using a 1D model, modelled the impact of a TEC array on sea bed morphodynamics in the Severn Estuary (Bristol Channel, UK). They found that maximum sea bed changes did not exceed 0.1 m in areas of strong tidal asymmetry over a lunar month, but bed changes were still noticeable even 50 km away from the array. Neill et al. [6,10] applied a 3D model and studied the impact of a large array of TECs (rated 300 MW) on the maintenance mechanisms of headland associated sandbanks in the Channel Islands. The maximum sea bottom change was ˜0.01 m in the vicinity of TECs and in a larger area (100 km^2), after half lunar month. Following on, Robins et al. [4] used a 2D model to study the effect of TEC arrays on sediment transport processes, in the Anglesey Skerries channel (Wales, UK). They found that the sediment transport capacity rates changed less than the natural variability range, for small array deployments of 10–50 MW. However, the changes exceeded the natural range for array sizes over 50 MW and changes were seen as far as 10 km away from TECs. On the other hand Fairley et al. [11,12] studied the cumulative impacts of 4 TEC arrays on sandbank dynamics of the Pentland Firth

* Corresponding author.
E-mail address: Antonia.Chatzirodou@uwe.ac.uk (A. Chatzirodou).

https://doi.org/10.1016/j.apor.2019.101882
Received 28 January 2019; Received in revised form 15 July 2019; Accepted 19 July 2019
Available online 05 August 2019

Fig. 1. a) Upper Figure: "The Pentland Firth site." W 4°30' - W 1°42' and N58°30'- N59°18'. Google Earth. Taken December, 2018; b) Upper left figure: "United Kingdom." W11°- W1° and N51°- N59°. Google Earth. Taken December, 2018; c) Lower Figure: "The Inner Sound channel." W 3°18' - W 2°58' and N58°37'48"- N58°43'48". Google Earth. Taken December 2018. White lines denote the extent of the sandbanks A, B, C found in Inner Sound.

(Scotland, UK), by using a 3D numerical model. The model output showed that bed level changes up to 0.2 m can occur at those sandbanks, which is not significant compared to natural changes, at least at this site. Martin-Short et al. [13] used a 2D model to investigate the impacts of TEC arrays on sediment carrying capacity of the Inner Sound Channel of Pentland Firth, UK. They found that arrays in excess of 85 turbines influenced bed shear stress patterns, concluding that the decelerated flows through TECs may deposit sediment from the edges of the Inner Sound towards its centre in array areas.

The present research used the Pentland Firth, Inner Sound channel (Scotland, UK) between the Scottish Mainland of the UK and the Island of Stroma (Fig. 1) as the test study site to investigate morphodynamic impacts of tidal energy extraction. The Inner Sound has been recognized as an excellent location for a commercial development of a TEC array by 2020 [14]. The proposed TEC array lies close to three large sandbanks. The objective of this study is to investigate the impacts of tidal energy extraction from a generic array of horizontal in-stream TECs on sediment dynamics and bed change of those sandbanks. A 3D hydro-morphodynamic model Delft3D [15] was set up for the Pentland Firth, Inner Sound channel. TECs effect was parameterized in the model as an added volumetric sink term in the momentum conservation equations. The thrust coefficient C_T, which represents the level of energy extraction from a TEC, is linked to the equivalent coefficient in the momentum sink term in Linear Momentum Actuator Disc Theory (LMADT) for energy reduction [16,17]. We modelled five energy extraction scenarios by using a range of thrust coefficients.

The paper is organised as follows: Section 2 gives a detailed description of the test study site; Section 3 describes the numerical model set up used in this study; Section 4 presents the most significant impacts of the TEC array on the hydrodynamic environment of the Inner Sound; Section 5 presents the effect of TECs on the morphodynamic environment of the sandbanks and Section 6 concludes the paper.

2. Field site: the Pentland Firth, Inner Sound channel

The Inner Sound channel in Pentland Firth separates the Island of Stroma and the north coast of Scottish Mainland (Fig. 1). Water depths between 25–30 m coupled with fast moving tidal flows found in the central parts of the channel, provide very favourable site characteristics for TEC deployments [18–20].

2.1. Hydrodynamic environment

Semi-diurnal tides are predominant in the Inner Sound, with the highest tidal range occurring to the west and the lowest to the east of the channel. Mean spring tidal range recorded at the nearest tidal gauge is 2.88 m. Due to different tidal ranges and phases at the ends of the PF channel, tidal currents of up to 8 ms^{-1} are generated in places in response to 2.5 m head drop during a tidal cycle. Maximum currents at flood phase travel north-east and at ebb phase north-west in the channel. Currents differ in strength and direction at each phase of the tidal cycle, indicating a significant tidal current asymmetry in large areas inside Inner Sound [21]. The residual currents over a tidal cycle confirm the presence of a large anticlockwise cyclonic eddy eastwards and a smaller scale clockwise anti cyclonic eddy westwards of the Inner Sound [22]. An energetic wave climate approaches the channel from the west but most areas in the middle and to the east side of the Sound appear to be more protected from incoming waves [23]. Water depth in the channel vary from ˜75 m below mean sea level (MSL) northward to ˜25–30 m in central areas.

2.2. Morphodynamic environment

Three large sandbanks (A, B and C) located in the Inner Sound channel dominate the local morphological environment [14]. The remaining areas are found to be largely bed rock (Fig. 1). The sandbanks predominantly consist of coarse sand and fine gravel with D50 values between 2–5 mm (British Geological Survey (BGS), 2013). The sediment transport and morphodynamic environment of those sandbanks have been extensively modelled using Delft-FLOW (MOR) in 3D, in Chatzirodou et al. [20,21] where a full description of the sediment dynamics and morphology change can be found. It was found that all three sandbanks are morphodynamically active under the prevailing natural hydrodynamic regime where Sandbank A is the most active while Sandbank C is the least active. Sediment transport rates of the order of 10^{-3} $m^3/m/s$ were modelled on both Sandbanks A and B at various phases of a tidal cycle. Over a period of two spring-neap tidal cycles, the cumulative bed changes were found to be up to 2 m.

Fig. 2 presents a conceptual model of the natural sediment pathways that occur on Sandbanks A and B [20,21]. Around the sandbank A, net bed load transport is present on the southern flank, at flood phase and on the northern flank, at ebb phase. The two net ebb- and flood-dominated sediment transport pathways create a convergent zone, where sediments rest towards the middle areas of the bank (Fig. 2upper). Erosion mostly occurs on the flank regions and accretion occurs towards the central parts of the sandbank. Around the sandbank B, net ebb transport is present on the western flank and net flood transport on the eastern flank. The two mobile zones create an inner boundary where sediments are deposited. Erosion mostly occurs on the western flank with sediments resettling towards the central and north-eastern parts of the sandbank (Fig. 2lower). The reader is further referred to Chatzirodou et al. [20] for a full description of sediment dynamics and morphology change of sandbanks under the natural hydrodynamic regime.

It is clear that sandbanks are the predominant feature of the natural sedimentary and ecological environment of this area. Therefore, any changes to the natural tidal regime due to TEC installations may have significant impacts on their sustainability and integrity and also on the existence of benthic communities found on them.

3. Numerical modelling methodology

3.1. Model description

The open source Delft3D FLOW module, including the morphology (MOR) suite used in this study utilizes a finite difference representation of the unsteady swallow water equations in 2D and 3D to compute sediment transport processes (bed load rates in present case) and morphological changes [15]. For the 3-D flow simulation the system of equations reads:

$$\frac{\partial \zeta}{\partial t} + \frac{\partial HU}{\partial x} + \frac{\partial HV}{\partial y} = 0 \tag{1}$$

$$\frac{\partial u}{\partial t} + u\frac{\partial u}{\partial x} + \upsilon\frac{\partial u}{\partial y} + \frac{\omega}{H}\frac{\partial u}{\partial \sigma} = -\frac{1}{\rho_O}P_x + F_x + M_x + \frac{1}{H^2}\frac{\partial}{\partial \sigma}\left(\nu^v\frac{\partial u}{\partial \sigma}\right) + f\upsilon \tag{2}$$

$$\frac{\partial \upsilon}{\partial t} + u\frac{\partial \upsilon}{\partial x} + \upsilon\frac{\partial \upsilon}{\partial y} + \frac{\omega}{H}\frac{\partial \upsilon}{\partial \sigma} = -\frac{1}{\rho_O}P_y + F_y + M_y + \frac{1}{H^2}\frac{\partial}{\partial \sigma}\left(\nu^v\frac{\partial \upsilon}{\partial \sigma}\right) - fu \tag{3}$$

where $u$and υ are the horizontal velocities in $-x$ and $-y$ direction; ω is the vertical velocity in σ -coordinates; P_x, P_y are the horizontal pressure gradients approximated by the Boussinesq assumptions; ρ_O is the reference density; F_x, $F_y$equal to the horizontal viscous forces presenting the unbalance of the horizontal Reynold's stresses; M_x, M_y are external forces added as source or sink terms in the momentum equations; $\nu^{v,back}$is the minimum background value for the vertical eddy viscosity; f presents the Coriolis parameter; ζ is the water level above the reference plane $\sigma = 0$ and $H$is the total water depth.

3.2. Multi-scale model domain set up and model parameters

The model domain extends from 58°00′N to 60°00′N and from 5°44′W to 1°32′W with grid resolution from 2000 m and 200 m in deeper areas in Pentland Firth (Domains A, B) to 20 m in Inner Sound (Domain C) (Fig. 3). Domains A, B and C run in a fully coupled mode with domain decomposition process [24]. The model domain is forced along the open boundaries (Fig. 3) by astronomic tidal elevations from the TPXO 7.2 Global Inverse Model [25], based on the major semi-diurnal (M2, S2, N2, K2) and diurnal (K1, O1, P1, Q1) tidal constituents. Model bathymetry data are provided by The Crown Estate (TCE), UK at a very fine grid resolution of 20 m x 20 m (Fig. 4).

The spatial resolution of the largest computational domain (Domain A) is 2 km while that of the Domain C is 20 m. The boundaries of Domain C were carefully selected to avoid any sediment influx or outflux. As the all seabed areas other than sandbanks consist of bedrock and are free of sediment, sediment transport takes place only in areas associated with sandbanks. The flow depth is divided into 10 sigma layers. The key model parameters were calibrated and validated using flow and water level measurements at a number of locations within the model domain. It was found that a Chézy bed friction coefficient of 50 $m^{1/2}$ s^{-1} and a horizontal eddy viscosity value of 5 m^2s^{-1} gave the best model performance. Considering the sediment transport regime and sediment sizes at site Van Rijn (1993) sediment transport formula is used. Focusing only on short term impacts the total simulation time of 30 days is used with simulation time step of 0.2 min. Model details and simulation conditions are summarized in Tables 1 and 2. Further details of the hydro-morphodynamic model setup and extensive model validation against hydrodynamics measured at and around the study site are found in Chatzirodou and Karunarathna [22] and [26]. Model validation reveals that it is capable of reproducing hydrodynamic conditions very accurately.

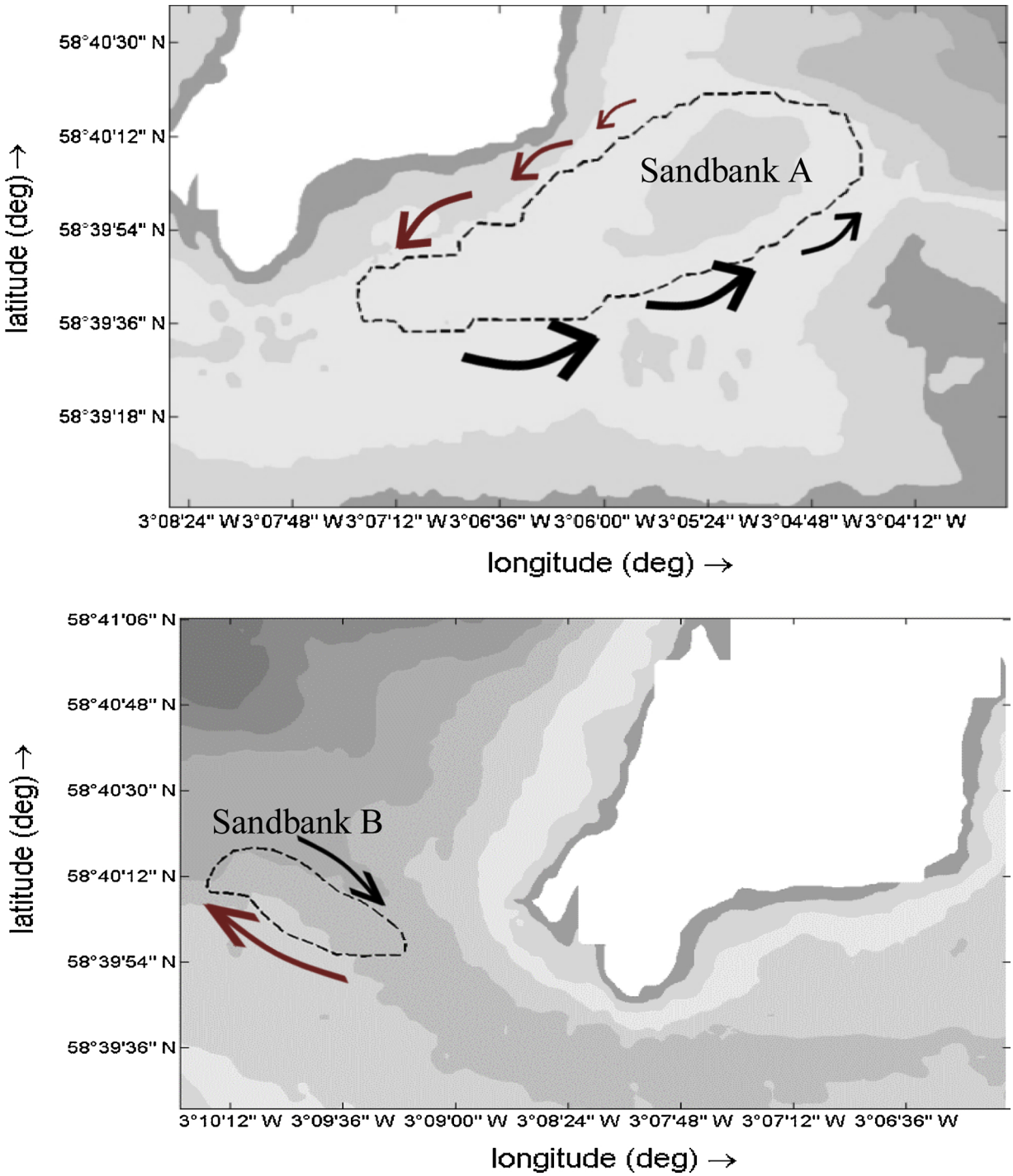

Fig. 2. Conceptual model of the sediment pathways occurring on the sandbanks A (upper) and B (lower) under natural tidal flows. Red and black arrows indicate the magnitude and direction of the ebb- and flood-dominated sediment transport patterns respectively.

3.3. Turbine representation in the model domain

TECs are included in the water column as porous discs, along the internal boundary of two computational grid cells, as devised by Delft3D modelling suite [24,27]. Delft3D FLOW module incorporates a porous disc (TEC) by adding a quadratic momentum loss term M_x, M_y in the right hand side of the horizontal momentum conservation equations 2, 3 [24]. For the rest of our description we will use the single term TEC.

The steady-state subcritical flow rate Q passing through the TEC region placed normal to the flow is related to the difference between the upstream and downstream water levels as follows [24]:

$$Q = \mu A_D \sqrt{2g\ |\zeta_u - \zeta_d|} \tag{4}$$

where A_D equals to the swept area of the TEC; μ presents a dimensionless contraction coefficient ($0 \leq \mu \leq 1$) and $|\zeta_u - \zeta_d|$ is the local water level difference between upstream and downstream of TEC. Power extraction by the turbine rotor from water is manifested as a pressure drop thus creating a lower velocity behind the rotor plane, which in turn manifests as a thrust force. Owing to the pressure drop, momentum is reduced. The pressure is assumed to be uniform over the area of the disc. Consequently, the control volume expands to satisfy

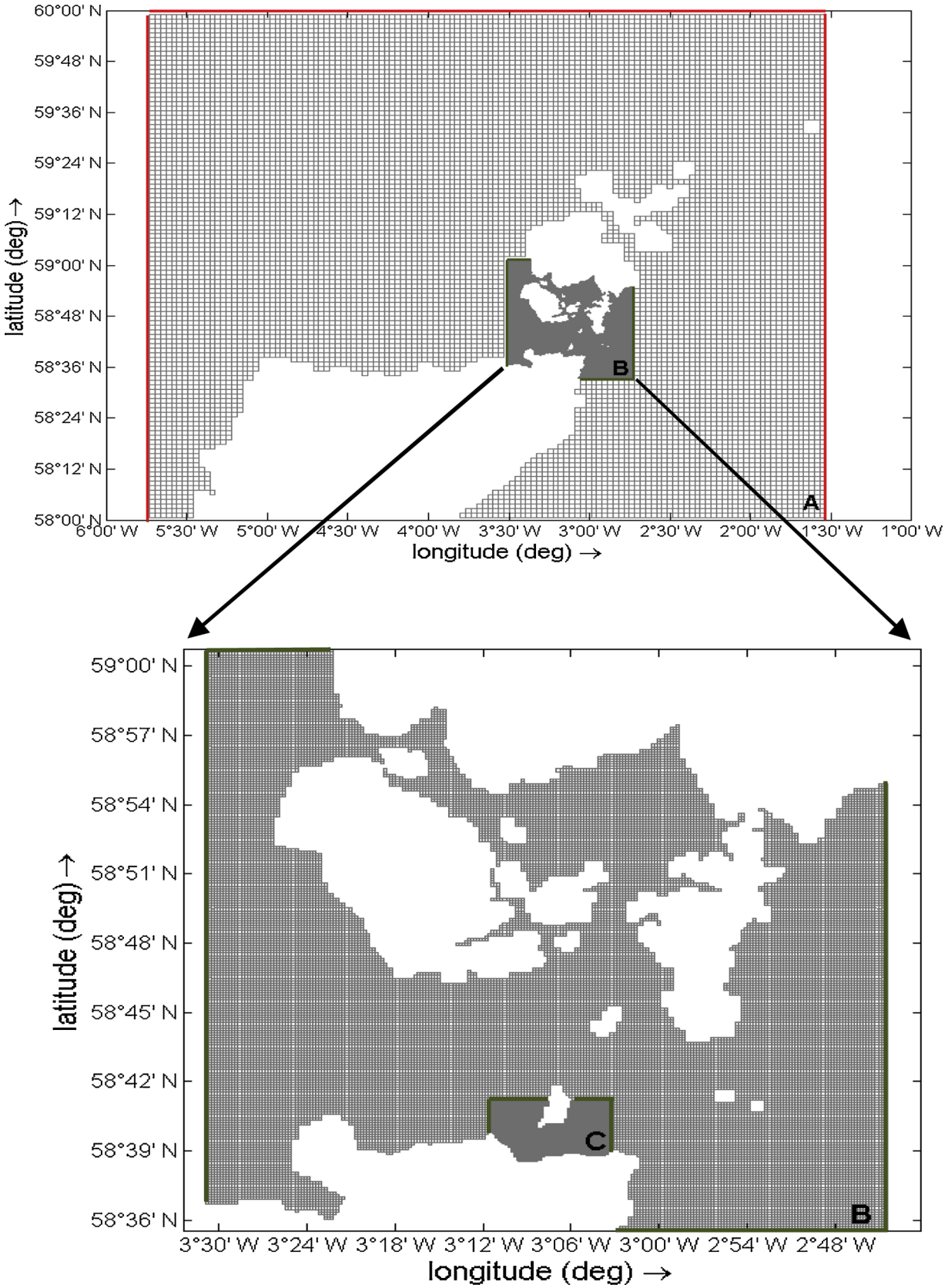

Fig. 3. Multi-scale computational domain set up. A: Large scale model covering the entire continental shelf (2 km x 2 km), B: Pentland Firth model (200 m x 200 m), C: Inner Sound channel model (20 m × 20 m). Red lines denote the open boundaries and green lines denote the coupled internal boundaries used in domain decomposition process.

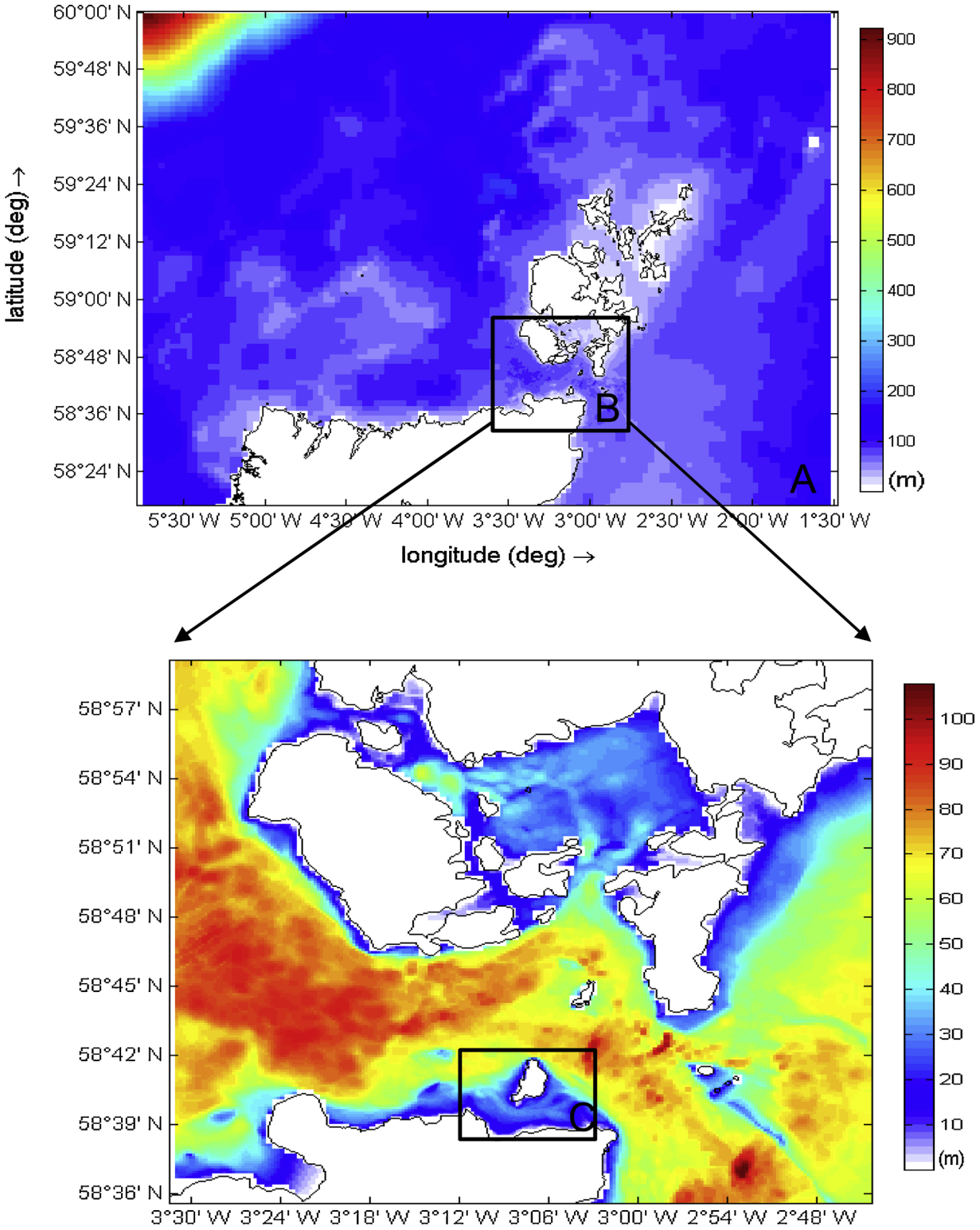

Fig. 4. Numerical bathymetry generation. The hydrodynamic grids (A, B, C) are mapped onto bathymetry data available at 20 m x 20 m grid resolution. The colour bars indicate the water depth values.

mass conservation thus inducing a wake. It is assumed that TEC is "sub-grid" and that the M_x retarding force felt by the flow, due to the deployment of a single TEC normal to the flow (in y- direction) will locally equilibrate with the pressure head drop as follows [24]:

$$M_x = \rho g \frac{|\zeta_u - \zeta_d|}{\Delta x} \tag{5}$$

Substituting $|\zeta_u - \zeta_d|$ term from Eq. (4) into Eq. (5), Eq. (5) becomes:

$$M_X = \rho \frac{Q^2}{2\mu^2 A_D^2 \Delta x} \tag{6}$$

Considering now $Q = U_{m,n} \mid \overrightarrow{U_{m,n}} \mid A_D$, Eq. (6) turns into:

Table 1
Delft3D FLOW parameters used in the hydrodynamic model set up of the study area.

Key Model Parameter	Value
Grid size	Domain A: 2 km × 2 km (2D) Domain B: 200 m × 200 m (3D) Domain C: 20 m × 20 m (3D)
Vertical distribution profile	10 even σ-layers
Simulation time	09/09/2001 - 09/10/2001
Time step	0.2 min
Chézy bed friction	50 $m^{1/2}$ s^{-1}
Background horizontal eddy viscosity $\nu_{H,back}$	Domain A: 10 m^2s^{-1} Domain B: 5 m^2s^{-1} Domain C: 1 m^2s^{-1}
Density	Barotropic
Turbulence Closure Model (TCM)	κ-epsilon

Table 2
Delft3D FLOW (MOR) parameters used in the morphodynamic model set up of the study area.

Key Parameter	Value
Mobile Sand Availability	Sandbanks A,B,C
Sediment transport formula	Van Rijn (1993) (only bed load rates)
SED_{50} (space-varying)	Sandbank A: 3 mm & 2 mm Sandbank B: 4 mm Sandbank C: 4.75 mm Non-erodible regions: 9mm
Initial sand layer thickness	Space-varying
Initial non-erodible layer thickness	Zero
Bed level updating	Yes (at each computational time step)

$$M_x = C_{loss-U}\rho\frac{U_{m,n} \mid \overrightarrow{U_{m,n}}\mid}{\Delta x} \tag{7}$$

in which $C_{loss-U} = \frac{1}{2}\left(\frac{1}{\mu^2}\right)$ is a constant uniform resistance coefficient term; $U_{m,n}$ is the horizontal velocity (x-component) normal to the submersed TEC (in y- direction) and $\mid \overrightarrow{U_{m,n}}\mid$ equals to the magnitude of the horizontal velocity (x-component) in each σ-layer occupied by the TEC. The C_{loss-U} coefficient should represent the properties of an actual TEC. We selected the most appropriate C_{loss-U} value by use of the Rankin-Froude LMADT principles which have been widely applied in literature [7,28–30] to parameterize the effects of horizontal in-stream TECs in 2D/3D shallow water numerical models. According to LMADT [16,17] (Fig. 5) the thrust force F_T felt by the flow, due to the presence of a TEC modelled as a porous disc is defined by:

$$F_T = \frac{1}{2}\rho A_D u^2 C_T \tag{8}$$

Where ρ is the water density, A_D is the swept area of the TEC, $C_T = 4a(1-a)$ determines the thrust coefficient of the TEC with $a = \frac{u-u_1}{u}$; and u is the free stream velocity upstream of the TEC region (Fig. 5). Reworking $C_T = 4a(1-a)$, the a factor is written in terms of the C_T coefficient as follows [31]:

$$a = \frac{1}{2}(1-\sqrt{1-C_T}) \tag{9}$$

By use of the definition of a factor and Eqs. (9) and (8) becomes:

$$F_T = \frac{1}{2}\rho A_D u_1^2 C \tag{10}$$

with:

$$C = \left[4\frac{1-\sqrt{1-C_T}}{1+\sqrt{1-C_T}}\right] \tag{11}$$

where C is a resistance coefficient, felt by the bypassing flow through the TEC region, for

each C_T value and u_1 is the horizontal velocity normal to the TEC (Fig. 5).

We combine Eqs. 7, 10 as follows:

$$M_{x,total} = \rho\frac{C_{loss-U}}{\Delta x}\left(\frac{1}{n}\right)\sum_{\sigma_{bottom}}^{\sigma_{surface}} U_{m,n} \mid \overrightarrow{U_{m,n}}\mid \tag{12}$$

$$M_{x,total} = \frac{1}{2}\rho u_1^2\frac{C}{\Delta x} \tag{13}$$

in which n equals to the total number of σ-layers occupied by the TEC area and $\sigma_{surface}$, σ_{bottom} present the upper and lower σ-layers expanding in the TEC region. By use of $\left[\left(\frac{1}{n}\right)\sum_{\sigma_{bottom}}^{\sigma_{surface}} U_{m,n} \mid \overrightarrow{U_{m,n}}\mid = u_1^2\right]$ equality in Eqs. (12) and (13), C_{loss-U} is defined as:

$$C_{loss-U} = \frac{1}{2}C = \frac{1}{2}\left[4\frac{1-\sqrt{1-C_T}}{1+\sqrt{1-C_T}}\right] \tag{14}$$

By selecting the thrust coefficient C_T for a real TEC replaced by a porous disc, we can assign a value to the C_{loss-U}. The thrust force felt by the flow in the TEC region is highly dependent on the C_{loss-U} and the inflow velocities. Similar quantities are defined for a single turbine located in

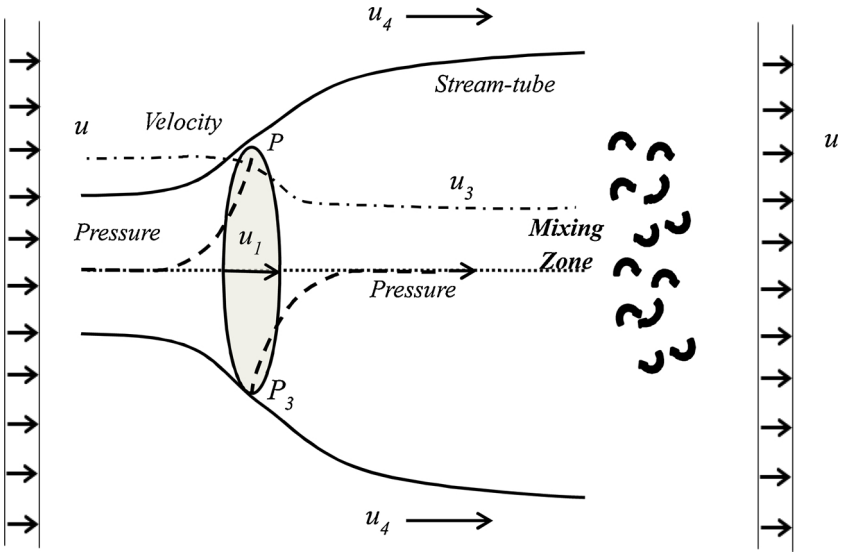

Fig. 5. Classic LMADT (Description of the properties of a TEC device in an unbounded flow pattern).

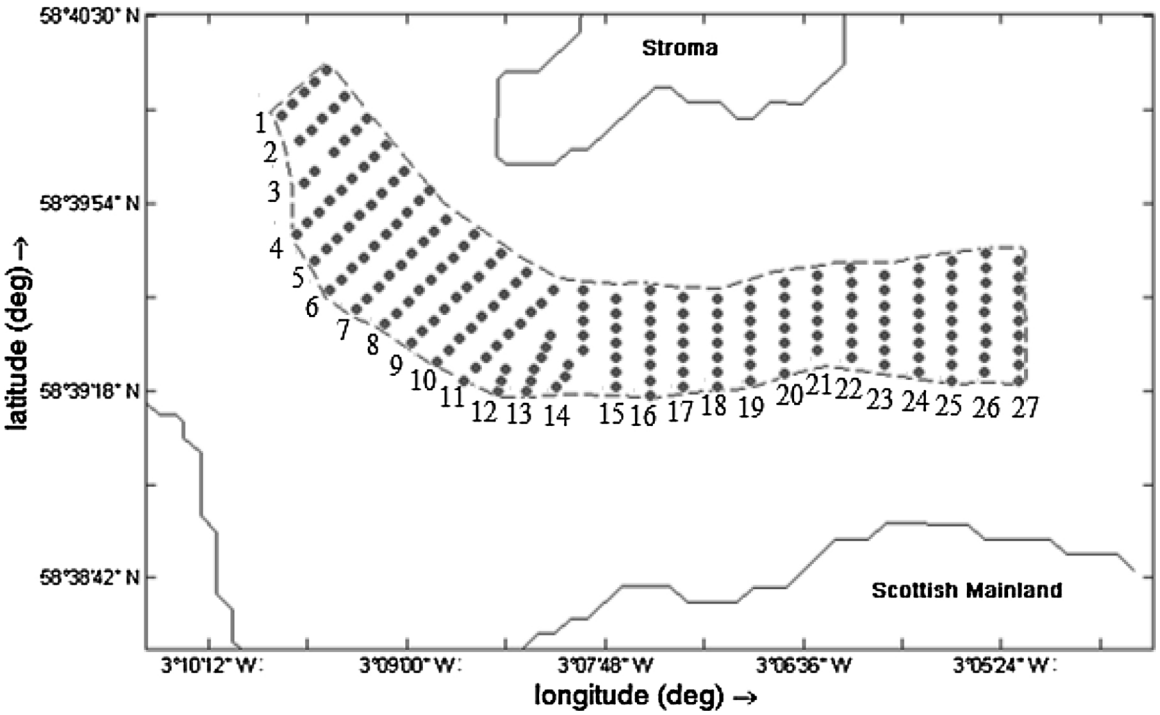

Fig. 6. TEC array configuration and row numbering used in the model.

the x- direction or along a line segment at an angle of an integer multiple of 45° with the x- direction to calculate C_{loss-V} and $C_{loss-U,V}$ coefficients respectively. However, it is worth noting that there are certain assumptions specific to the TEC representation as a porous disc inside the model domain and these are summarized as follows; A physical porous disc introduces higher turbulent intensity values inside the wake, directly downstream from the disc region, in contrast to a porous disc modelled in the Delft3D FLOW module [29,32]; The horizontal grid size is larger than the vertical grid size, thus the TEC is represented by a rectangular rather than a circular shape in the water column [33]; The width of the vertical σ-layers varies according to each phase of the tidal cycle. As a result, the modelled TECs will rise and fall slightly in the water column at flood and ebb phase. The swept area of a TEC will further increase at flood tide and decrease at ebb tide, due to σ-grid vertical discretization. However, for calculations, it is assumed that the swept area is the same throughout the tidal cycle [34]; Variable C_T represented by C_{loss-U} are not supported in the Delft3D FLOW module, thus a constant coefficient is chosen for each energy extraction scenario. It is also assumed that a TEC will produce energy even at the lowest and highest tidal currents, since 'cut in' and 'cut off' velocities for TECs in operation are not included in computations; The scale of the processes modelled is in order of few hundred meters. Therefore, the model is reliable to evaluate far-field instead of near- field effects. Finally, TECs are assumed to be of horizontal-axis type. Most of the full-scale demonstration devices operate with a horizontal-axis rotation which suggests them as the most promising design to date [35]. Also, TECs support structures effects are not included in the model.

3.4. Modelled tidal energy extraction scenarios

In 2010 the Crown Estate leased a number of sites for tidal stream energy development projects in the Pentland Firth and Orkney Waters (PFOW) in the UK, with a potential total power generation capacity of 1.6 GW [36]. Amongst potential developers MeyGen Limited was awarded an Agreement for Lease (AFL) to develop a 400 MW horizontal-axis TEC array by 2020 in Inner Sound Channel [14]. In the present study, impacts of a generic TEC array on the morphodynamics of the MeyGen lease site in the Inner Sound are modelled. To develop the TEC array, 28 rows with 200 TECs of 20 m diameter (D) turbines were added to the model in a staggered arrangement (Fig. 6). It should be noted that both the TEC array and turbine characteristics used in this research do not correspond to any real tidal energy development project however, values used represent the most commonly considered turbine and array scenarios studied to-date.

In Fig. 6, row numbers (RN) have been assigned to the array configuration to be able to comment on the results shown and discussed in Section 5. We ensured that each TEC occupied one grid cell in the model domain to account for possible interactions between TECs within the array, still though to a limited extent considering simplicity of the energy extraction model (see limitations of the model in Section 3.3). For generic array and device conditions, intra-row spacing is set to 2.5D and array-row spacing to 10D [37]. In the vertical water column, a minimum of 5 m top and bottom clearance is allowed [37]. To represent different levels of energy extraction, five scenarios (SA-SE) were modelled with a gradual increase in C_T, from a minimum (0.18) to a maximum (0.85) value assigned to each scenario. The selection of the thrust coefficient is based on Waldman et al. [38] and [39]. All scenarios tested with C_T and equivalent $C_{loss-U,V}$ are summarized in Table 3. The maximum C_T value of 0.85 is used as this is the value that has been agreed from the generic TEC ($D = 20$ m) thrust curve, at a rated current speed of 2.5 ms^{-1} to be used in wave and tidal energy developments sites in the Pentland Firth [40]. It should also be noted that no experimental results were available in present study for further C_T evaluation.

Table 3
Modelled tidal energy extraction scenarios inside the Inner Sound channel.

a/a	Scenarios	C_T	$C_{loss-U,V}$
0	NE	–	–
1	SA	0.18	0.10
2	SB	0.45	0.30
3	SC	0.64	0.50
4	SD	0.77	0.70
5	SE	0.85	0.90

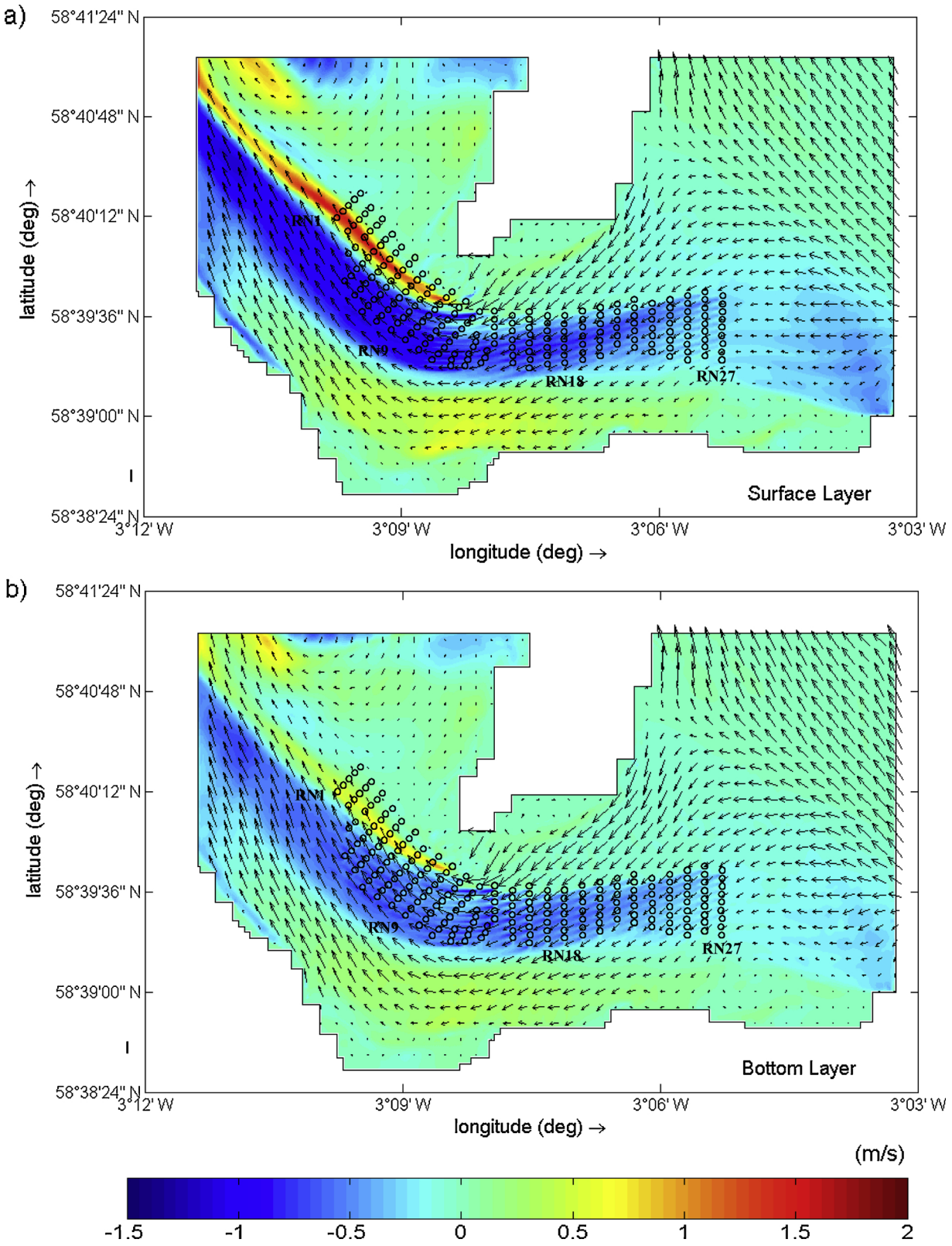

Fig. 7. Differences in horizontal velocities (m/s) between 'worst case' SE scenario and 'no energy extraction' NE scenario at spring ebb phase (19/09/2001 02:40), at a) the surface and b) the bottom layer. The colour bar indicates the magnitude of velocity differences and arrows indicate altered velocity vectors of the 'worst case' SE scenario. Grey circles denote TECs location. For full row numbering refer to Fig. 6.

In the analysis given in Section 5, the main focus is to identify the effects on the hydrodynamics and sandbank morphodynamics in the Inner Sound, resulting from the highest energy extraction (SE) scenario ('worst case') relative to the 'no energy extraction (NE)' scenario and then to investigate the extent of the effects of other scenarios (SA-SD) when compared to the 'worst-case'.

4. Three dimensional hydrodynamic effects of TEC array in the Inner Sound

This section describes the effects of 'worst case' energy extraction scenario on the three-dimensional hydrodynamic regime of the Inner Sound, focusing on the areas where sandbanks are located. The altered

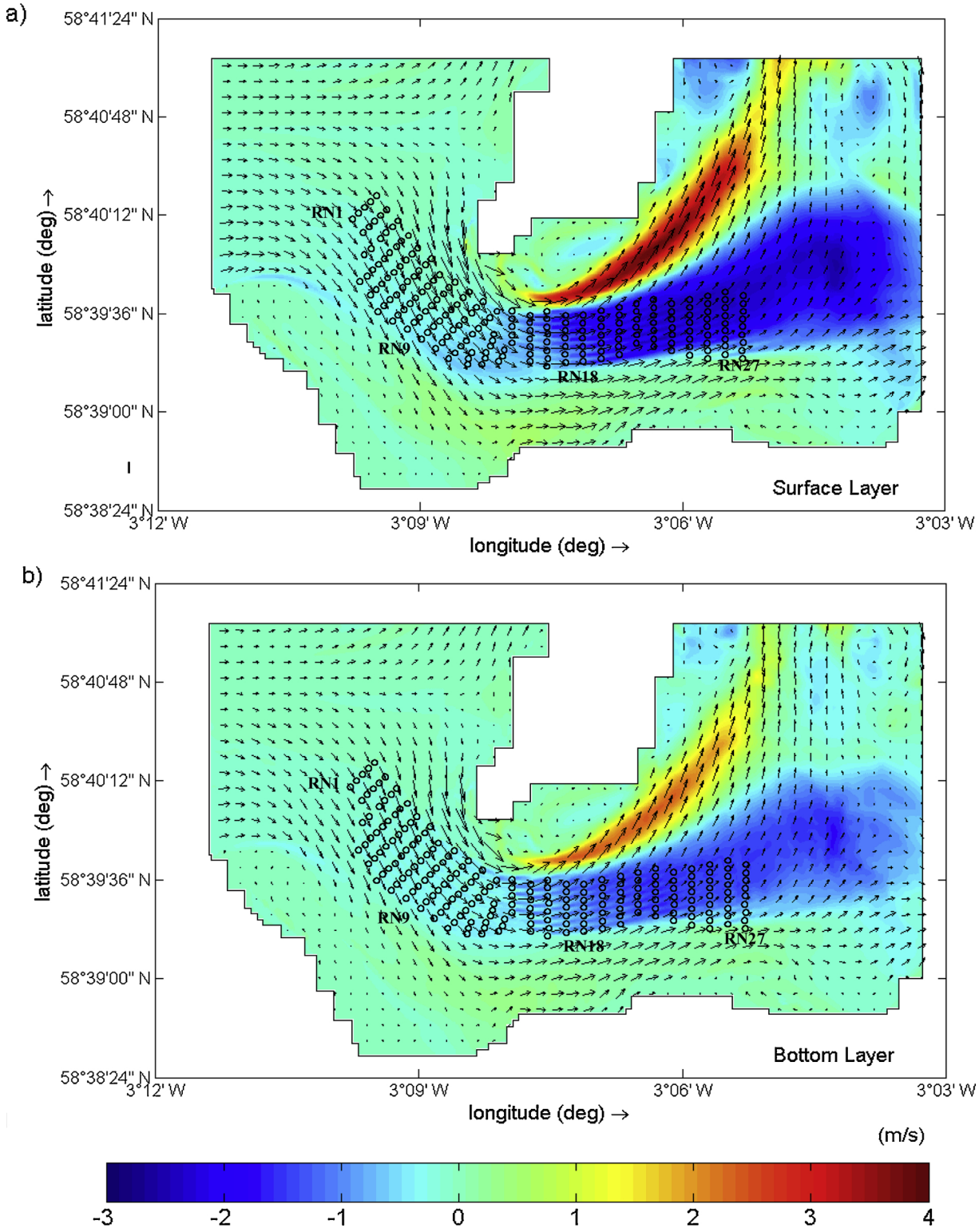

Fig. 8. Differences in horizontal velocities (m/s) between 'worst case' SE scenario and 'no energy extraction' NE scenario (SE-NE) at spring flood phase (19/09/2001 08:00), at a) the surface and b) the bottom layer. The colour bar indicates the magnitude of velocity differences and arrows indicate altered velocity vectors of the 'worst case' SE scenario. Grey circles denote TECs location. For full row numbering refer to Fig. 6.

transient and residual (mean) tidal flows in the Inner Sound at the maximum spring tide on 19/09/2001are presented and discussed.

4.1. Effects on tidal hydrodynamics

Figs. 7 and 8(a, b) show the differences in surface and bottom horizontal velocities between SE and NE scenarios (SE-NE), at spring ebb and flood phases. Positive values indicate increase in current speed while negative values indicate reduction as a result of energy extraction. At ebb phase (19/09/2001 02:40) maximum surface currents passing through RN 1-10 of the array are highly affected where velocity reduction as a result of energy extraction reaches 1.5 ms^{-1}. Surface velocities to the north of RN 1-10 are approximately four times higher when energy is extracted, increasing up to 1.6 ms^{-1} and by less than 0.8 ms^{-1} to the south of the array. To satisfy volume conservation, surface velocities decrease by up to ~ 25% with 1.2 ms^{-1} loss in the west array-wake region and 0.8 ms^{-1} loss in the east array-wake region (Fig. 7a). The spatial distribution of change of ebb current patterns at the surface and bottom as a result of energy extraction remains the same although surface velocity magnitudes have changed more than the bottom velocities. Bottom velocities increase approximately three times by up to 0.9 ms^{-1} in the north-west part of the array and less than 0.6 ms^{-1} at the southern array boundary. Maximum velocity decrease as a result of energy extraction in the westward wake region is 0.9 ms^{-1}(~ 23% from NE currents) (Fig. 7b).

It is worth noting that the changes in free surface levels between SE and NE at ebb (not shown) are very low compared to the mean spring tidal range of ~2.88 m and local depths of ~25-75 m. Ebb tide water levels decrease by less than 19 cm to the south-west, close to the Scottish mainland and increase by up to 8 cm towards the north-west exit of the Inner Sound channel. This results agree with previous studies done elsewhere, where surface elevation differences between energy extraction and no energy extraction were found to be not significant [e.g. 5,7,28,41–43].

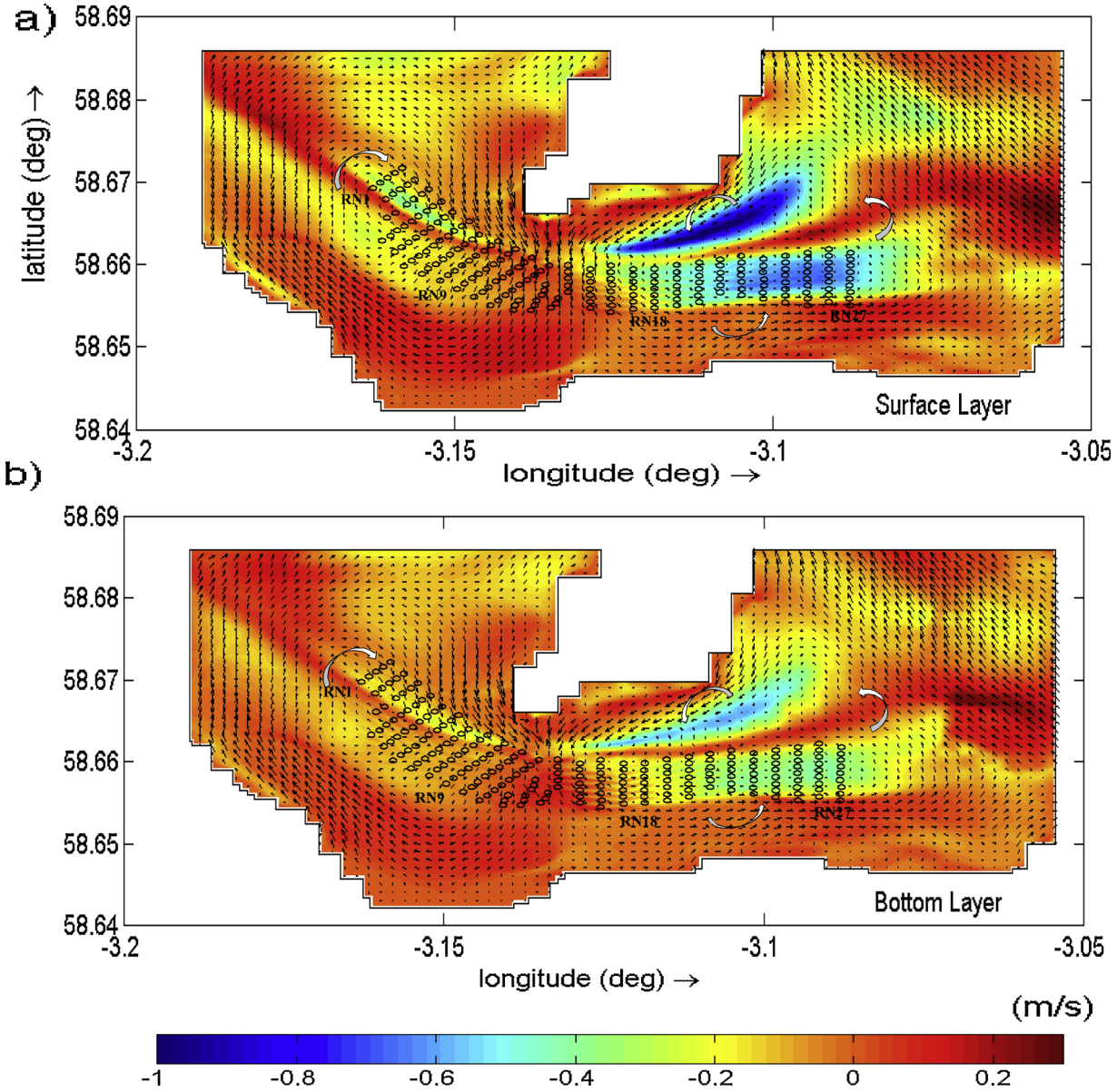

Fig. 9. Differences in residual velocities (m/s) between 'worst case' SE scenario and 'no energy extraction' NE scenario (SE-NE) over a spring tidal cycle (19/09/2001), at a) the surface and b) the bottom layer. The colour bar indicates the magnitude of velocity differences and arrows indicate altered velocity vectors of the 'worst case' SE scenario. White arrows indicate the rotational direction of the residual eddies of the 'worst case' SE scenario. Grey circles denote TECs location. For full row numbering refer to Fig. 6.

At flood phase (19/09/2001 08:00) (Fig. 8a,b), the maximum differences between the currents for SE and NE scenarios are seen closer to RN 15–20 of the array, where highest amount of energy is extracted from the north-east part of the array. Surface free stream velocities are approximately 6.6 times higher, increased by over 3.3 ms^{-1} in the lee of the Island of Stroma and by 1.9 ms^{-1} towards the North-East. Surface velocities have decreased up to 55%, with 3 ms^{-1} loss in the east array-wake region (RN 15–27) and 0.6 ms^{-1} in the west array-wake region (RN 1–14) (Fig. 8a). Similar to the ebb phase, the spatial distribution of change of flood current at the surface and bottom layers is similar. Bottom free-stream currents increase around 6.6 times by up to 2.5 ms^{-1} north-eastward of the TEC array and 0.35 ms^{-1} southward, close to Scottish mainland as a result of energy extraction. Maximum velocity reduction in the east array-wake region is close to 1.7 ms^{-1} (˜ 55%) (Fig. 8b).

The differences in free surface flood levels between SE and NE scenarios are higher than that at ebb phase. Flood tide water levels increase up to a maximum of 36 cm towards the south-east exit of the Inner Sound and decrease up to 24 cm to the north-east exit of the channel. However, it can still be considered insignificant, compared to the deep water depths in this region.

4.2. Effects on residual tidal flows

Residual tidal flows are important for sediment transport. Fig. 9(a, b) shows the differences in surface and bottom residual (mean) currents, between the SE and NE scenarios, over a tidal cycle at maximum spring tide (19/09/2001) where the currents can be the highest. Surface residual currents decrease by up to 0.6 ms^{-1} (˜ 90%) through the east part of the TEC array (RN 22–27) as a result of energy extraction. The most significant surface residual flow velocity reduction is seen to the north of the east part of the TEC array (RN 16–25), at the lee of Island of Stroma, where velocity is reduced by up to 1.0 m/s as a result of energy extraction. Despite local variations in residual currents

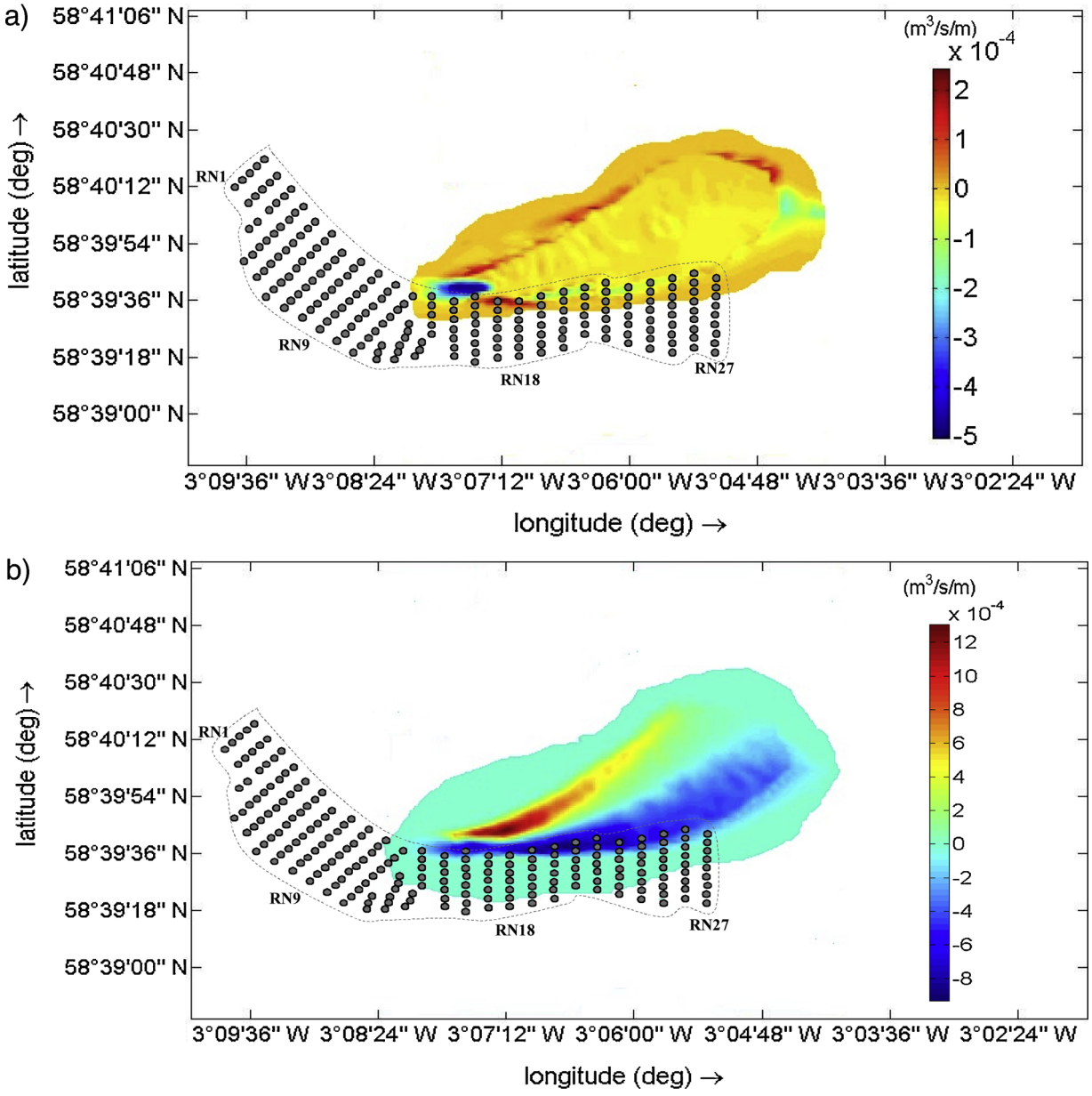

Fig. 10. Differences in bed load transport rates ($m^3/s/m$) between 'worst case' SE and 'no energy extraction' NE scenarios (SE-NE); at maximum spring (19/09/2001) a) ebb (02:40) and b) flood (08:00) tide on the sandbank A. The colour bar indicates the magnitude of sediment transport rates differences. The dashed grey line and grey circles denote the extent of the TEC array layout and the position of TECs. For full row numbering refer Fig. 6.

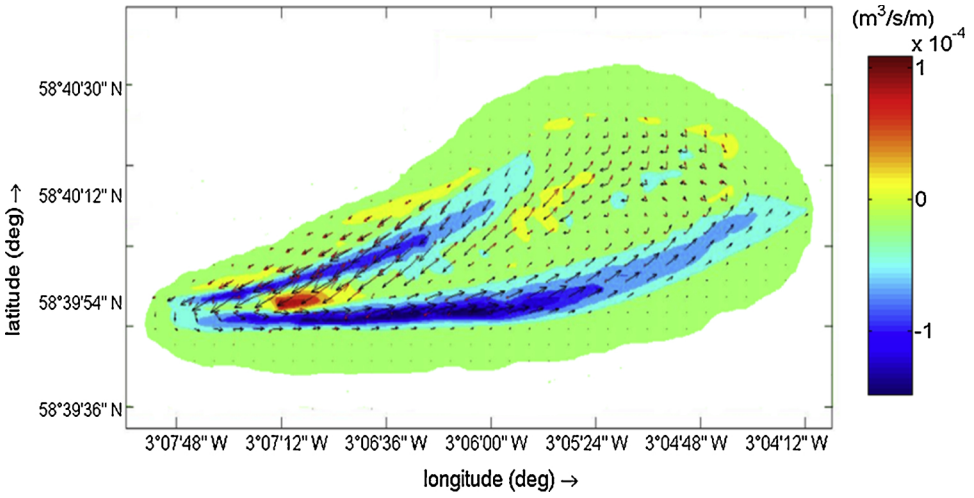

Fig. 11. Differences in residual bed load transport rates ($m^3/s/m$) between 'worst case' SE and 'no energy extraction' NE scenarios (SE-NE), over the tidal cycle at maximum spring tide (19/09/2001), on the sandbank A. The colour bar indicates the magnitude of sediment transport rates differences. The red and black arrows define the sediment transport vectors at 'worst case' SE and 'no energy extraction' NE scenarios respectively.

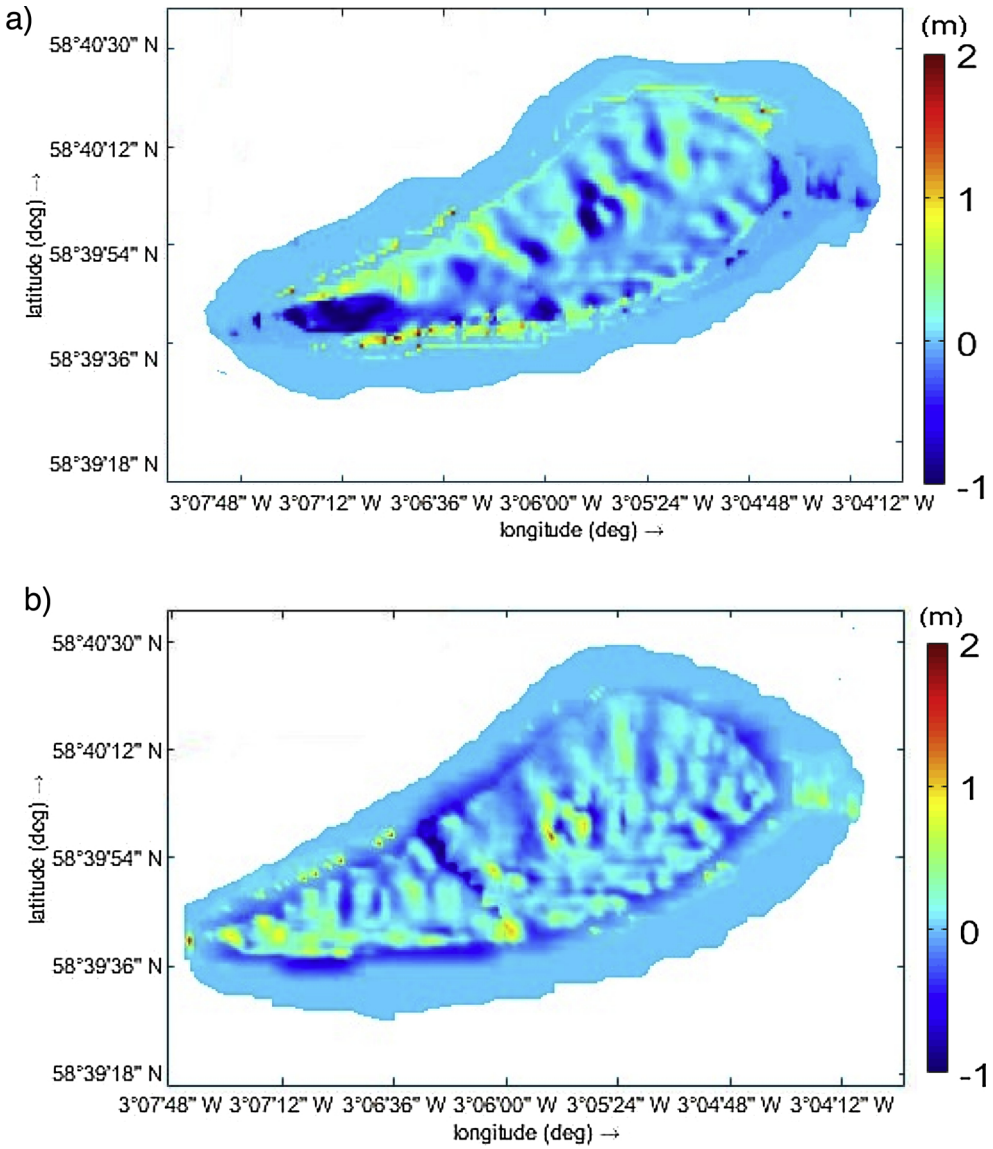

Fig. 12. a) Differences in sea bed change (m) between 'worst case' SE and 'no energy extraction' NE (SE-NE) scenarios, at the end of one month simulation period (from 09/09/2001 to 09/10/2001), on sandbank A. b) Natural sea bed change (m) at 'no energy extraction' NE scenario, at the end of one month simulation period (from 09/09/2001 to 09/10/2001), on sandbank A.

through west TECs, the residual anti-cyclonic eddy observed westward in Inner Sound at NE scenario [26] is still maintained.

The effects of energy extraction on bottom residual flows also are more pronounced at the eastern side of the array where a velocity reduction in the array region (RN 20–27) of around 0.4 ms^{-1} and to the north of the array of up to 0.6 ms^{-1} can be seen. The spatial variability of the surface and bottom residual current change as a result of energy extraction is very similar.

5. Effects of TECs on sandbanks dynamics in the inner sound

Changes to the transient and residual tidal currents can change sediment dynamics of the sedimentary areas of the Inner Sound. In the analysis presented below the effects of TECs on tidally driven sandbank dynamics in the Inner Sound are described, taking the' worst case' SE scenario. The cumulative effects of sediment transport over the simulation period of one month on the morphology of the sand banks A, B and C are discussed in terms of total bed level change of each sandbank.

5.1. Sandbank A: effects on sediment transport patterns and morphology change

Sandbank A is located to the eastern side of the turbine array considered in this study. Fig. 10 shows the differences in bed load transport rates on the sandbank A between 'worst case' SE and 'no energy extraction' NE scenarios (SE-NE) at spring ebb and flood phases. At maximum ebb phase (19/09/2001 2:40) a notable decrease of ~ 85% in bed load transport rates on the west wedge of the sandbank A as a result of energy extraction can be seen (Fig. 10a). As a result of localised increase in current velocities (see Section 4.1), sediment transport rates increase by a factor of 2.5 at the south-west and north flank of the sandbank, while minor reductions in transport rates are observed further upstream at the eastern flank. It is important that despite the observed variations in sediment transport rates, ebb dominant sediment transport patterns on the sandbank A remain unaffected (Fig. 10a). At maximum flood phase (19/09/2001 08:00), sediment transport rates at the northern part of sandbank A increase while that at the southern part

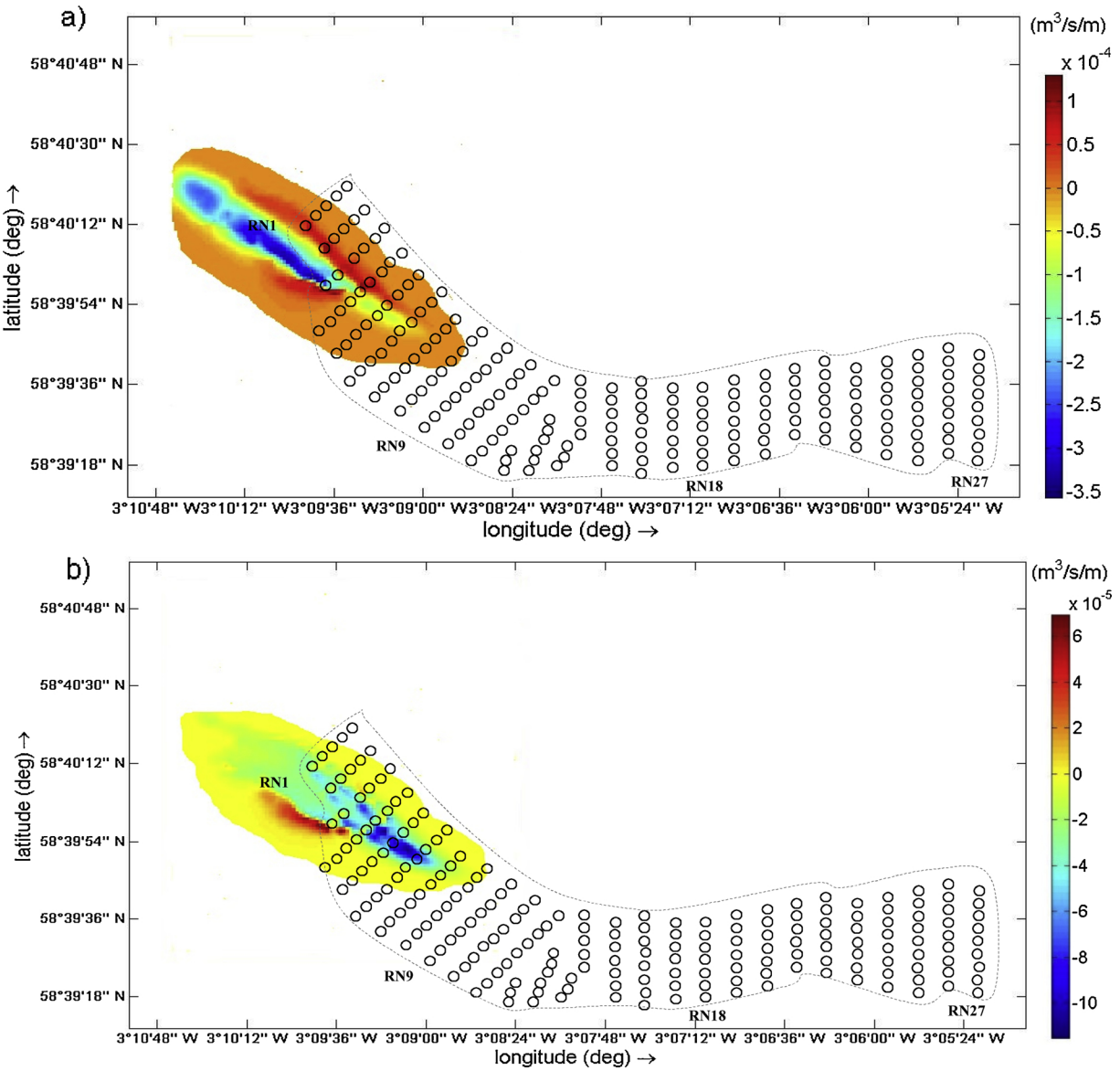

Fig. 13. Differences in bed load transport rates (m^3/s/m) between 'worst case' SE and 'no energy extraction' (SE-NE) scenarios, at maximum spring (19/09/2001) a) ebb (02:40) and b) flood (08:00) tide, on the sandbank B. The colour bar indicates the magnitude of sediment transport rates differences. The dashed grey line and grey circles denote the extent of the TEC array layout and the position of TECs. For full row numbering refer Fig. 6.

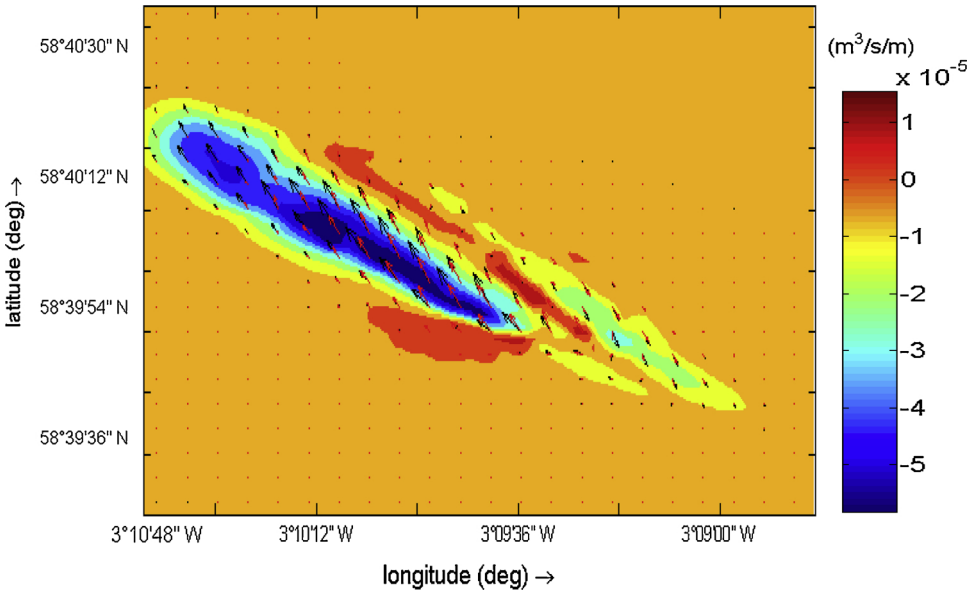

Fig. 14. Differences in residual bed load transport rates ($m^3/s/m$) between 'worst case' SE and 'no energy extraction' NE (SE-NE) scenarios, over the tidal cycle at maximum spring tide (19/09/2001), on the sandbank B. The colour bar indicates the magnitude of sediment transport rates differences. The red and black arrows define the sediment transport vectors at 'worst case' SE and 'no energy extraction' NE scenarios respectively.

reduce, showing a clear boundary of erosion and deposition regions (Fig. 10b).

Fig. 11 shows the differences in residual bed load transport rates on the sandbank A between 'worst case' SE and 'no energy extraction' NE scenarios over the tidal cycle at maximum spring tide (19/09/2001). Two clear regions of decrease of residual transport can be seen. Comparison between SE and NE shows that residual transport decreased by up to 67% in the north-west region of the sandbank. The change in residual transport then led to areas of erosion and deposition of the sandbank. The maximum cumulative accretion and erosion at the end of one month simulation period (09/09/2001-09/10/2001) were 0.8 m and 1.0 m respectively (Fig. 12a). Erosion and accumulation were localised to different areas of the sandbank however, it can be seen that the bed level change of the sandbank as a result of energy extraction is significant. In Fig. 12b, cumulative natural sea bed change on sandbank A over the same period is shown. Comparison of Fig. 12a and b confirms that natural sediment dynamics and spatial distribution of accretion/erosion of sandbank A are significantly affected by the TEC array although the scale of change remains largely unaffected.

5.2. Sandbank B: effects on sediment dynamics and morphology change

Sandbank B is located at the western fringe of the turbine array. Fig. 13 shows the differences in bed load transport rates on the sandbank B between 'worst case' SE and 'no energy extraction' NE scenarios at spring ebb and flood phases. At maximum ebb phase (19/09/2001 2:40), bed load transport rates decrease by about 54% on the west flank of the sandbank, due to flow deceleration downstream of the TECs as a result of energy extraction (RN 4–14). Bed load transport rates increase by a factor of 1.8 in the middle south-westward area and across the eastern flank of the sandbank (Fig. 13a), following local increases in current velocities (see Section 4.1). However, despite the observed changes in transport rates, ebb dominant spatial sediment transport patterns on the sandbank B are not significantly affected by tidal energy extraction.

At maximum flood phase (19/09/2001 08:00), sediment transport rates decrease as a result of energy extraction almost at the entire sandbank area with transport rate diminishing up to 50% across the south-eastern flank, as a result of flow deceleration through the west array-wake region. Bed load transport rates increase by a factor of 2.3 on a small area towards south-westwards of the sandbank (Fig. 13b). It is important that despite the observed changes in transport rates, naturally occurring spatial sediment transport patterns are maintained, similar to what observed in sandbank A.

In order to investigate potential bed level changes that can occur as a result of energy extraction, residual bed load transport rates over one tidal cycle are studied. Fig. 14 shows the differences in residual bed load transport rates between the 'worst case' SE and 'no energy extraction' NE scenario over the tidal cycle at maximum spring tide (19/09/2001) on the sandbank B. Residual ebb transport rate decreases by up to 66% on the west flank followed by localised increases in the south-west part and across the eastern flank. On the other-hand residual flood transport rates decrease by up to 54% south-eastward on the sandbank (Fig. 14). Overall, residual sediment transport rates have decreased in most areas of sandbank B.

As can be seen in both Figs. 14 and 15a, decreasing residual ebb transport rates on the west flank and the southern side of sandbank B lead to maximum accretion of 0.8–1.0 m between 'worst case' SE and 'no energy extraction' NE scenarios, at the end of one-month simulation period (09/09/2001-09/10/2001). Likewise, decreasing flood transport rates result in maximum cumulative accretion of 0.5 m across the eastern flank. A cumulative erosion of up to 0.20 m in the central part of the sandbank and by up to 0.7 m on the north-west flank (Fig. 15a) can also be seen. Overall, the peripheral areas of sandbank undergo accretion while middle parts erode as a result of tidal energy extraction. Fig. 15b shows natural cumulative sea bed change of sandbank B during the same simulation period. Comparison of Fig. 15a and b shows that sandbank B has become more morphodynamically active under the new hydrodynamic regime created by energy extraction and that spatial erosion/accretion areas have almost flipped sides.

5.3. Sandbank C: effects on sediment transport patterns and bed form dynamics

The small sandbank C is located in a region of weak flow separation, in the lee side of the Island of Stroma. Minor differences in the residual sediment transport rates at spring tide (19/09/2001) are observed between the' worst case' SE and the 'no energy extraction' NE scenarios leading to cumulative changes in sediment thickness of less than 0.14 m over the whole sandbank C area at the end of one month's simulation (09/09/2001-09/10/2001) (Figs. 16 and 17). In majority of the sandbank area, the differences in sea bed change between SE and NE are negligible (less than 0.02 m). Therefore, it is fair to say that the sandbank C is almost unaffected by tidal energy extraction.

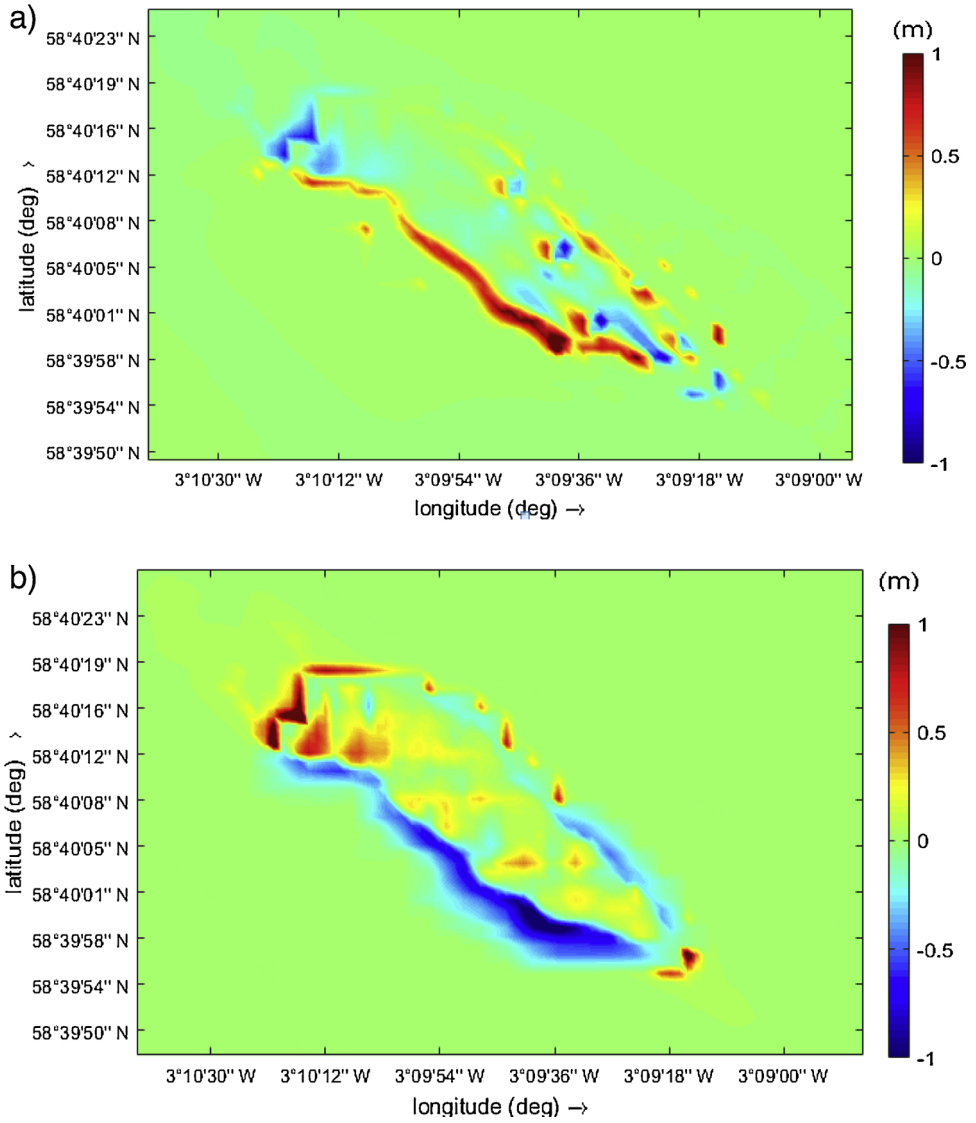

Fig. 15. a) Differences in sea bed change between 'worst case' SE and 'no energy extraction' NE (SE-NE) scenarios, at the end of one month period (from 09/09/2001 to 09/10/2001), on the sandbank B. b) Natural sea bed change (m) at 'no energy extraction' NE scenario, at the end of one month simulation period (from 09/09/2001 to 09/10/2001), on sandbank B.

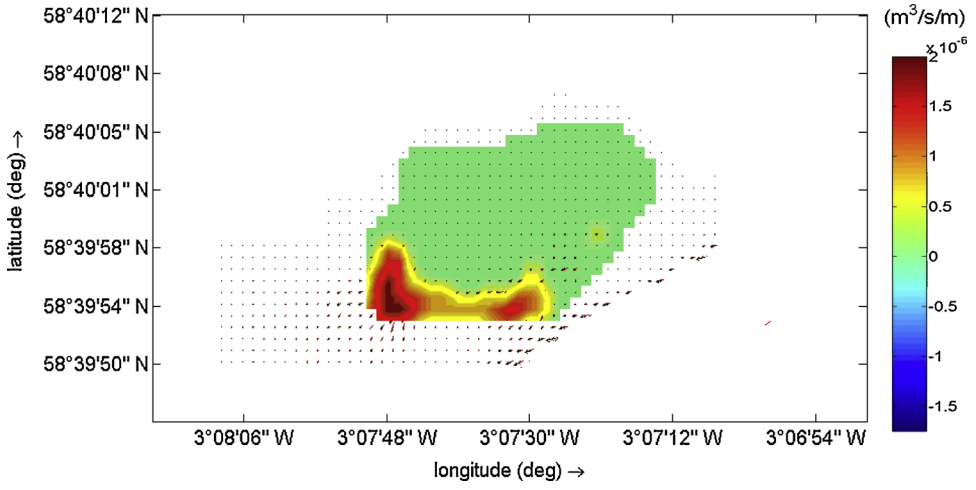

Fig. 16. Differences in residual bed load transport rates ($m^3/s/m$) between 'worst case' SE and 'no energy extraction' NE (SE-NE) scenarios, over a spring tidal cycle (19/09/2001), on the sandbank C. The colour bar indicates the magnitude of sediment transport rates differences. The red and black arrows define the sediment transport vectors at 'worst case' SE and 'no energy extraction' NE scenarios respectively.

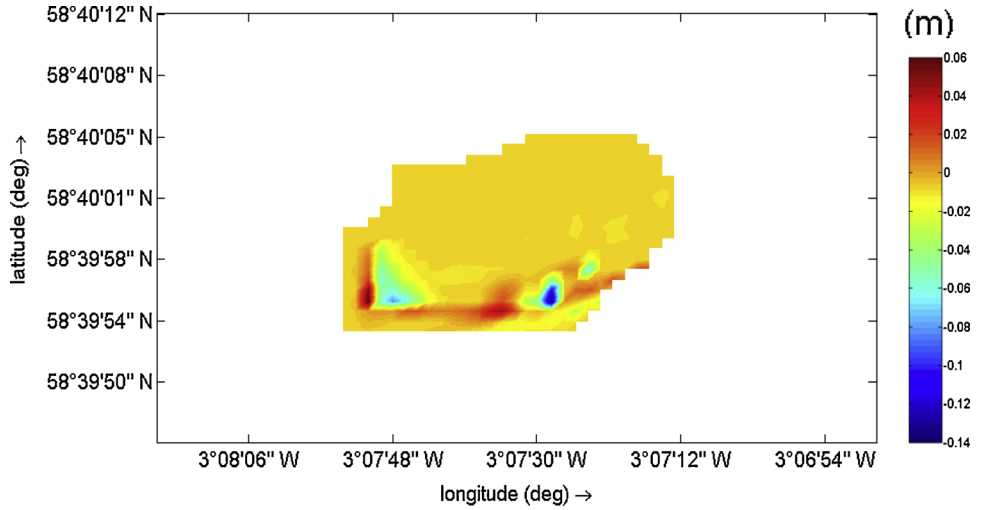

Fig. 17. Differences in sediment thickness (m) between 'worst case' SE and 'no energy extraction' NE (SE-NE) scenarios, at the end of one-month period (from 09/09/2001 to 09/10/2001), on the sandbank C.

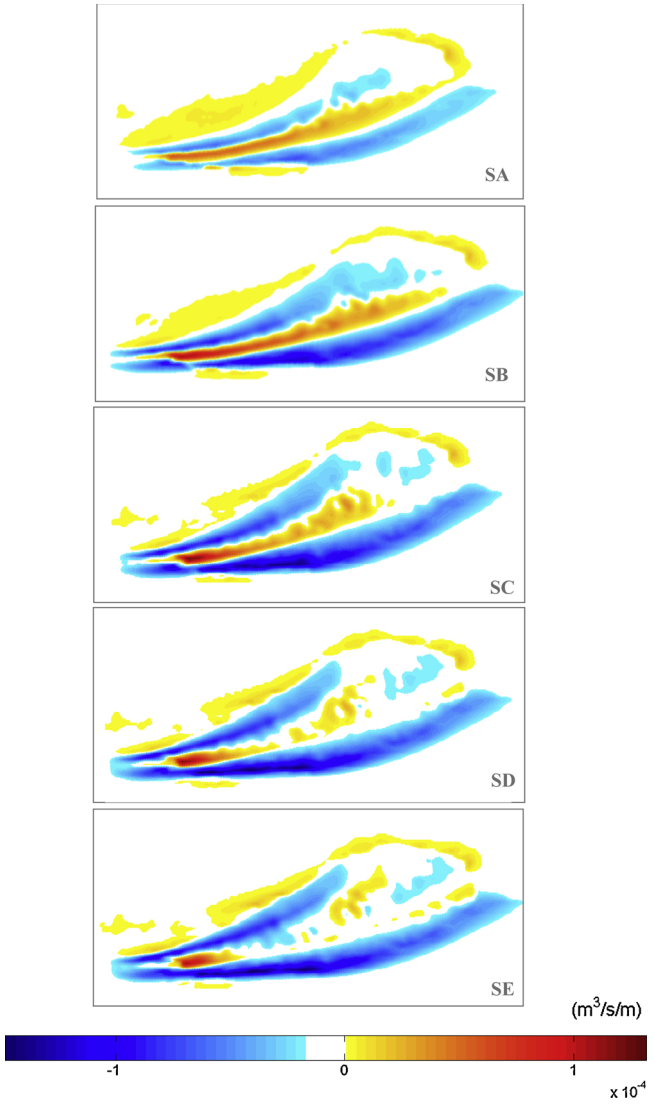

Fig. 18. Differences in residual bed load transport rates ($m^3/s/m$) between each tidal energy extraction scenario (SA-SE) and the 'no energy extraction' scenario (NE), over the tidal cycle at maximum spring tide (19/09/2001), on the sandbank A.

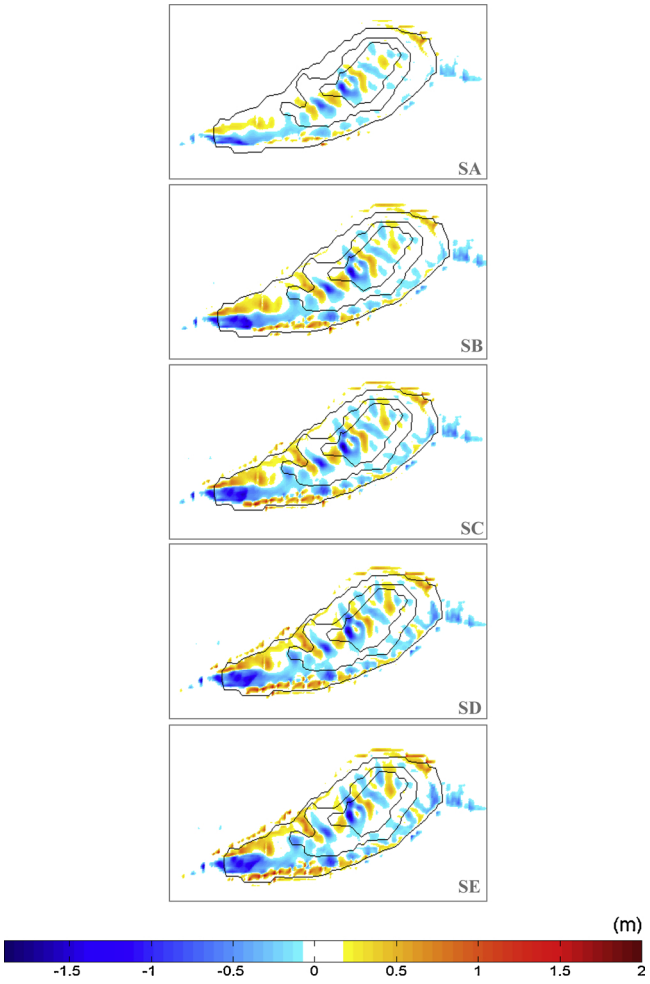

Fig. 19. Differences in sea bed change (m) between each tidal energy extraction scenario (SA-SE) and the 'no energy extraction' scenario (NE), at the end of the one-month simulation period (from 09/09/2001 to 09/10/2001), in the sandbank A.

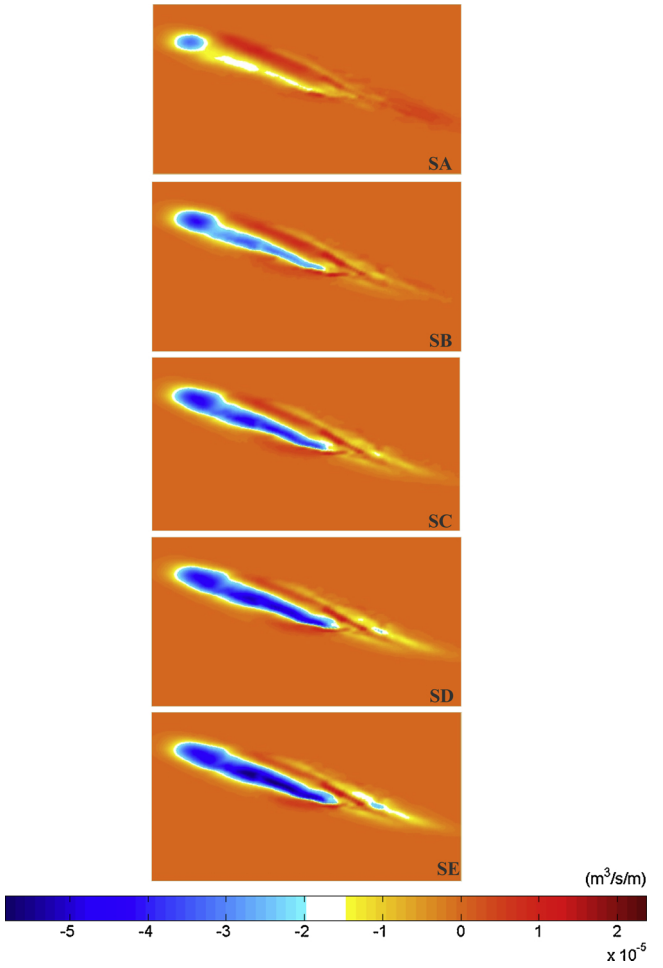

Fig. 20. Differences in residual bed load transport rates ($m^3/s/m$) between each tidal energy extraction scenario SA-SE and the 'no energy extraction' scenario NE, over a spring tidal cycle (19/09/2001), on the sandbank B.

5.4. Comparisons of the impacts of TECs on sandbank dynamics between the modelled tidal energy extraction scenarios

Results and analysis presented in this section focus on a comparison of sediment dynamics and sea bed change of sandbanks A and B under different tidal energy extraction scenarios modelled in this study. The presented results are from the one-month simulation time between 09/09/2001 and 09/10/2001, which covers two spring-neap tidal cycles, as in previous sections. This comparison will enable insights into how much energy can be extracted without imposing significant impacts on the sedimentary environment of the Inner Sound channel.

The differences in the residual bed load transport rates between each of the modelled energy extraction scenarios (SA-SE) and the 'no energy extraction' scenario (NE) were calculated at maximum spring tide (19/09/2001) on the sandbank A (Fig. 18). From SB to SE scenario residual sediment transport rate increases by a factor of approximately 4–5 towards the west wedge and decreases by up to 80–90% across the southern flank (Fig. 18). As a result of changes in residual sediment transport rate, the central areas of Sandbank A predominantly erode significantly while the flanking regions accrete (Fig. 19). The average changes in sediment thickness are around 0.43-0.69 m, exceeding the natural sea bed variability of 0.30-0.35 m, after one month simulations [20].

As can be seen in both Figs. 18 and 19, the effects of tidal energy extraction are minor for the SA scenario and become increasingly important for SB to SE scenarios. It proves that sediment dynamics of the sandbank A are sensitive to the level of energy extraction.

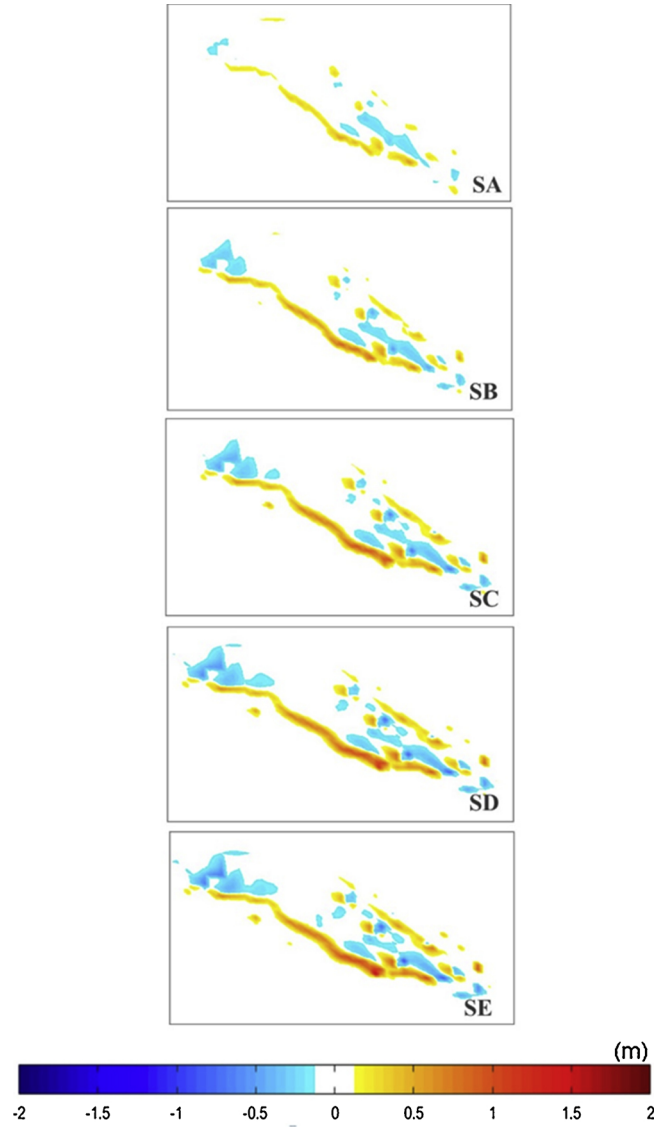

Fig. 21. Differences in sea bed change (m) between each tidal energy extraction scenario (SA-SE) and the 'no energy extraction' scenario NE, at the end of the one month period (from 09/09/2001 to 09/10/2001), on the sandbank B.

The differences in residual bed load transport rates between each of the modelled energy extraction scenarios (SA-SE) and the 'no energy extraction' scenario (NE) were also calculated at maximum spring tide (19/09/2001) on the sandbank B (Fig. 20). For the SC-SE scenarios residual sediment transport decreases by up to 38–66% respectively on the west flank.

Fig. 21 shows change in sediment layer thickness of Sandbank B after a one moth simulation period similar to Sandbank A. As a result of changes in residual sediment transport under SC-SE scenarios, the western flank of Sandbank B accretes while the middle areas are subjected to erosion. It is important to note that the average change in sediment layer thickness in one month is around 0.28-0.57 m, which does not exceed the natural sea bed variability of 0.47–0.52 m [26].

6. Summary and conclusions

A Delft3D hydro-morphodynamic model was set up to explore possible impacts of TEC array deployments on sediment dynamics and sea bed morphology. This study exemplifies the use of numerical models to study the effect of TEC arrays in greater detail. Although it is not possible to validate the model against tidal energy extraction, the

model was extensively validated against hydrodynamic conditions measured in and around the field site, acquiring the confidence of using the model for this study. The model is extremely useful to gain preliminary insights into the impacts of tidal energy harvesting as field or large-scale laboratory investigations are hardly possible to investigate impacts of TEC arrays on sediment dynamics. Same modelling techniques can be adopted and applied to undertake similar studies worldwide where tidal energy resource exploitation is possible. Such type of studies can help investigate detailed effects of TECs on the surrounding complex coastal environment and support decision-making process in renewable energy industry prior to reaching commercialization.

In here, the Inner Sound channel in Pentland Firth located between the Scottish Mainland and the Island of Stroma (UK) was used as the test study site, as this site is already licensed for a large marine energy development. TECs effect was parameterized in the model, as an added volumetric sink term in the momentum conservation equations and the properties of an actual TEC device were linked to the equivalent momentum sink term, by the use of the Linear Momentum Actuator Disc Theory (LMADT) principle. To represent different levels of energy extraction, five scenarios (SA-SE) were modelled with a gradual increase in TEC thrust coefficient C_T, from a minimum (0.18) to a maximum (0.85) value uniformly assigned to TECs at each scenario. The limitations in the model in terms of TEC device representation should be acknowledged however, it should be noted that the focus of this study is on large scale sediment dynamics due to flow alteration by energy harvesting than the turbulent scale local sediment movement due to turbine wakes.

The dynamics of sandbanks A, B, C are governed by the highly energetic tidal flows found in the channel which were significantly affected by tidal energy extraction. Their very own existence is strongly linked with the island associated flow dynamics of the existing tidal regime [21]. Therefore, it is not surprising that any form of change to the current flow field potentially will change the dynamics of them. For the 'worst case' SE scenario, tidal currents decreased in the array areas and further upstream and downstream from the array, both at peak ebb and flood phase. However, the water levels over a full tidal cycle presented minor changes. The main residual current circulation observed at the 'no energy extraction' scenario was also largely unaffected by energy extraction. However, the anticlockwise cyclonic eddy observed eastwards expanded significantly over a larger area inside the channel following energy extraction. Although the deployment of the TEC array significantly altered the existing hydrodynamic regime at the close proximity to the array, it is still important to note that the magnitude and the nature of changes will depend on the tidal phase and the locality with respect to the array.

The effects of the TEC array on the sediment dynamics and morphology of sandbanks A, B and C were then investigated by comparing the sediment transport rates and bed changes occurring under the 'worst case (SE)' scenario and the 'no energy extraction' (NE) scenario. A one-month simulation period covering two spring and neap tidal cycles was used. The changes were also compared with the natural changes that will occur over the same simulation period. The model results reveal that both Sandbanks A and B are sensitive to tidal energy extraction and that morphological changes following energy extraction far exceeds the natural changes during the same simulation period. The morphological changes of sandbank C are not significant. The severity of sediment movement and bed change of sandbanks A and B depends on the level of energy extraction where trust coefficients of until 0.45 did not have a noticeable effect on the morphodynamics.

If changes to sediment dynamics and hence morphology of sandbanks A and B accumulates over a long period of time, it may be possible that sandbank A will be relocated further northwards in Inner Sound. Also, any short or long-term changes to sandbank morphology may disturb the benthic ecology of these delicate sediment systems, which may need time to adjust to a new flow environment. Further research should be carried out to investigate these aspects in detail and to explore potential impact mitigation mechanisms.

It should be noted that this study did not consider any specific turbine type. The energy extraction scenarios investigated do not replicate any specific potential future development. Also, although the wake behind TECs and supporting structures of bottom mounted TECs may have some impacts on very localised morphodynamics of the TEC array site, considering the focus of this study is at a more wider scale morphodynamics of the Inner Sound channel, wake effects were not taken into account.

Any changes to the seabed sediment environment may be of significance to complex ecological system that prevail in deep sea sandbanks where they are used as habitat and breeding grounds by numerous marine species. Therefore, potential shift of the existing natural environment may affect these species and a wider chain of marine habitat.

Acknowledgements

HK and AC acknowledge the financial support provided by the TeraWatt (EP/J010170/1) and EcoWatt2050 (EP/K012851/1) projects funded by the Engineering and Physical Science Research Council of the United Kingdom. AC acknowledges the support of College of Engineering of Swansea University and EA/Welsh Government funded Low Carbon Research Institute for the studentship provided to pursue her PhD research at Swansea University.

References

[1] M.A. Shields, D.K. Woolf, E.P.M. Grist, S.A. Kerr, A.C. Jackson, ... J. Side, Marine renewable energy: the ecological implications of altering the hydrodynamics of the marine environment, Ocean Coast. Manage. 54 (2011) 2–9, https://doi.org/10.1016/j.ocecoaman.2010.10.036.

[2] D. Fallon, M. Hartnett, A. Olbert, S. Nash, The effects of array configuration on the hydro-environmental impacts of tidal turbines, Renew. Energy 64 (2014) 10–25, https://doi.org/10.1016/j.renene.2013.10.035.

[3] J.J. Waggitt, B.E. Scott, Using a spatial overlap approach to estimate the risk of collisions between deep diving seabirds and tidal stream turbines: a review of potential methods and approaches, Mar. Policy 44 (2014) 90–97, https://doi.org/10.1016/j.marpol.2013.07.007.

[4] P.E. Robins, S.P. Neill, M.J. Lewis, Impact of tidal-stream arrays in relation to the natural variability of sedimentary processes, Renew. Energy 72 (2014) 311–321, https://doi.org/10.1016/j.renene.2014.07.037.

[5] Z. Defne, K.A. Haas, H.M. Fritz, Numerical modeling of tidal currents and the effects of power extraction on estuarine hydrodynamics along the Georgia coast, USA, Renew. Energy 36 (2011) 3461–3471, https://doi.org/10.1016/j.renene.2011.05.027.

[6] S.P. Neill, J.R. Jordan, S.J. Couch, Impact of tidal energy converter (TEC) arrays on the dynamics of headland sandbanks, Renew. Energy 37 (2012) 387–397, https://doi.org/10.1016/j.renene.2011.07.003.

[7] M. Sánchez, R. Carballo, V. Ramos, G. Iglesias, Tidal stream energy impact on the transient and residual flow in an estuary: a 3D analysis, Appl. Energy 116 (2014) 167–177, https://doi.org/10.1016/j.apenergy.2013.11.052.

[8] I. Masters, A. Williams, T. Nick Croft, M. Togneri, M. Edmunds, et al., A comparison of numerical modelling techniques for tidal stream turbine analysis, Energies 8 (2015) 7833–7853, https://doi.org/10.3390/en8087833.

[9] S.P. Neill, E.J. Litt, S.J. Couch, A.G. Davies, The impact of tidal stream turbines on large scale sediment dynamics, Renew. Energy 34 (2009) 2803–2812, https://doi.org/10.1016/j.renene.2009.06.015.

[10] S.P. Neill, R. James, J.C. Scott, Impact of tidal stream turbines on sand bank dynamics, Paper Presented at World Renewable Energy Congress (2011).

[11] I. Fairley, I. Masters, H. Karunarathna, The cumulative impact of tidal stream turbine arrays on sediment transport in the Pentland Firth, Renew. Energy 80 (2015) 755–769, https://doi.org/10.1016/j.renene.2015.03.004.

[12] I. Fairley, I. Masters, H. Karunarathna, Sediment transport in the Pentland Firth and impacts of tidal stream energy extraction, September, Paper Presented in the 11th European Wave and Tidal Energy Conference (2015).

[13] R. Martin-Short, J. Hill, S.C. Kramer, A. Avdis, P.A. Allison, M.D. Piggott, Tidal resource extraction in the Pentland Firth, UK: potential impacts on flow regime and sediment transport in the Inner Sound of Stroma, Renew. Energy 76 (2015) 596–607, https://doi.org/10.1016/j.renene.2014.11.079.

[14] MeyGen, MeyGen Coastal Processes Modelling: Modelling Setups, Calibration and Results Incl. Addendum. A Final Report, Report No. SG5390 MeyGen Coastal Processes DHI Water & Environment (S) Pte. Ltd., Singapore, 2012.

[15] G.R. Lesser, J.A. Roelvink, J.A.T.M. Van Kester, G.S. Stelling, Development and validation of a three-dimensional morphological model, Coast. Eng. 51 (2004) 883–915, https://doi.org/10.1016/j.coastaleng.2004.07.014.

[16] R.E. Froude, On the part played in propulsion by differences of fluid pressure,

Trans. Inst. Naval Arch. 30 (1889) 390–405.
[17] W.J.M. Rankine, On the mechanical principles of the actions of propellers, Trans. Inst. Naval Arch. 6 (1865) 13–39.
[18] M.C. Easton, D.K. Woolf, S. Pans, An operational hydrodynamic model of a key tidal-energy site: inner Sound of stroma, Pentland Firth (Scotland, UK), October, Paper Presented in the 3rd International Conference on Ocean Energy (2010).
[19] L.M. Goddijn-Murphy, D.K. Woolf, M. Easton, Current patterns in the Inner Sound (Pentland Firth) from underway ADCP data, J. Atmos. Oceanic Technol. 30 (2013) 96–111, https://doi.org/10.1175/JTECH-D-11-00223.1.
[20] A. Chatzirodou, H. Karunarathna, D.E. Reeve, Investigation of deep sea shelf sandbank dynamics driven by highly energetic tidal flows, Mar. Geol. 380 (October) (2016) 245–263, https://doi.org/10.1016/j.margeo.2016.04.011 2016, ISSN 0025-3227.
[21] A. Chatzirodou, H. Karunarathna, D.E. Reeve, Modelling the response of subtidal sandbank dynamics to tidal energy extraction, Paper Presented in the 36th IAHR World Congress (2015).
[22] A. Chatzirodou, H. Karunarathna, Impacts of tidal energy extraction on sea bed morphology, Proceedings of 34th Conference on Coastal Engineering 1 (34) (2014) 33, https://doi.org/10.9753/icce.v34.sediment.33 Seoul, S. Korea.
[23] UK Hydrographic Office (UKHO), Admiralty Tide Tables, Volume 1 – United Kingdom and Ireland (including European Channel Ports), Hydrographer of the Navy, Great Britain, 2005.
[24] Deltares, Delft3D-FLOW Simulation of Multi-Dimensional Hydrodynamic Flows and Transport Phenomena, Including Sediments User Manual (Hydro-Morphodynamics) Version 3.15, Deltares, Delft, 2011.
[25] G.D. Egbert, A.F. Bennett, M.G.G. Foreman, TOPEX / POSEIDON tides estimated using a global inverse model, J. Geophys. Res. 99 (1994) 24821–24852, https://doi.org/10.1029/94JC01894.
[26] A. Chatzirodou, H. Karunarathna, D.E. Reeve, Modelling 3D hydrodynamics governing island-associated sandbanks in a proposed tidal stream energy site, Appl. Ocean. Res. 66 (2017) 79–94.
[27] X. Sun, J.P. Chick, I.G. Bryden, Laboratory scale simulation of energy extraction from tidal currents, Renew. Energy 33 (6) (2008) 1267–1274.
[28] V. Ramos, R. Carballo, M. Álvarez, M. Sánchez, G. Iglesias, Assessment of the impacts of tidal stream energy through high - resolution numerical modeling, Energy 61 (2013) 541–554, https://doi.org/10.1016/j.energy.2013.08.051.
[29] T. Roc, D.C. Conley, D. Greaves, Methodology for tidal turbine representation in ocean circulation model, Renew. Energy 51 (2013) 448–464, https://doi.org/10.1016/j.renene.2012.09.039.
[30] Y. Chen, B. Lin, J. Lin, S. Wang, Effects of stream turbine array configuration on tidal current energy extraction near an island, Comput. Geosci. 77 (2015) 20–28, https://doi.org/10.1016/j.cageo.2015.01.008.
[31] M.O.L. Hansen, N.N. Sørensen, R.G.J. Flay, Effect of placing a diffuser around a wind turbine, Wind. Energy 3 (2000) 207–213, https://doi.org/10.1002/we.37.
[32] M.E. Harrison, W.M.J. Batten, A. Myers, S. Bahaj, A comparison between CFD simulations and experiments for predicting the far wake of horizontal axis tidal turbines, September, Paper Presented at the 8th European Wave and Tidal Energy Conference (2009).
[33] S. Draper, Tidal Stream Energy Extraction in Coastal Basins (Doctoral dissertation). Retrieved from, (2011) http://www.eng.ox.ac.uk/civil/publications/theses/draper.pdf.
[34] S. Serhadlıoğlu, T.A.A. Adcock, G.T. Houlsby, S. Draper, A.G.L. Borthwick, Tidal stream energy resource assessment of the Anglesey Skerries, Int. J. Mar. Energy 3–4 (2013) 98–111, https://doi.org/10.1016/j.ijome.2013.11.014.
[35] Ng Kai-Wern, L. Wei-Haur, N.G. Khai-Ching, 2002–2012: 10 years of research progress in horizontal-axis marine current turbines, Energies 6 (2013) 1497–1526, https://doi.org/10.3390/en6031497.
[36] The Crown Estate, UK Wave and Tidal Key Resource Areas Project. Technical Methodology Report, Retrieved May 7, 2014, from (2013) http://www.thecrownestate.co.uk/media/395109/uk-wave-and-tidal-keyresource-areas-technological-report.pdf.
[37] The European Marine Energy Centre Ltd. (EMEC), Assessment of Tidal Energy Resource, Marine Renewable Energy Guides, Retrieved June 2, 2015, from file: (2009) http://www.emec.org.uk/assessment-of-tidal-energy-resource/.
[38] S. Waldman, S. Baston, R. Nemalidine, A. Chatzirodou, V. Venugopal, J. Side, Implementation of tidal turbines in MIKE 3 and Delft3D models of Pentland Firth & Orkney Waters, Coast. Ocean Manage. (2017), https://doi.org/10.1016/j.ocecoaman.2017.04.015.
[39] A. Pacheco, O. Ferreira, Hydrodynamic changes imposed by tidal energy converters on extracting energy on a real case scenario, Appl. Energy 180 (2016) 369–385.
[40] TeraWatt, TeraWatt Position Papers. A “toolbox” of Methods to Better Understand and Asses the Effects of Tidal and Wave Energy Arrays on the Marine Environment, Retrieved from, 1st ed., (2015) http://www.masts.ac.uk/media/35656/position_papers_terawatt_e-book.pdf.
[41] R. Ahmadian, R.A. Falconer, Assessment of array shape of tidal stream turbines on hydro-environmental impacts and power output, Renew. Energy 44 (2012) 318–327, https://doi.org/10.1016/j.renene.2012.01.106.
[42] D.R. Plew, C.L. Stevens, Numerical modelling of the effect of turbines on currents in a tidal channel – tory Channel, New Zealand, Renew. Energy 57 (2013) 269–282, https://doi.org/10.1016/j.renene.2013.02.001.
[43] J. Thiébot, P. Bailly du Bois, S. Guillou, Numerical modeling of the effect of tidal stream turbines on the hydrodynamics and the sediment transport – application to the Alderney Race (Raz Blanchard), France, Renew. Energy 75 (2015) 356–365, https://doi.org/10.1016/j.renene.2014.10.021.